Fortschritt-Berichte VDI

VDI

Reihe 17

Biotechnik/
Medizintechnik

M. Sc. Ben Nikolas Bufe,
Duisburg

Nr. 296

Method for Non-Invasive Skin Artifact-Free Spatial Bone Motion Tracking Using Pressure Sensor Foils

Method for Non-Invasive Skin Artifact-Free Spatial Bone Motion Tracking Using Pressure Sensor Foils

Der Fakultät für Ingenieurwissenschaften, Abteilung Maschinenbau und

Verfahrenstechnik der

Universität Duisburg-Essen

zur Erlangung des akademischen Grades

eines

Doktors der Ingenieurwissenschaften

Dr.-Ing.

genehmigte Dissertation

von

Ben Nikolas Bufe

aus

Hamburg, Deutschland

Referent: Prof. Dr.-Ing. Andrés Kecskeméthy

Korreferent: Prof. Janet Lenore Ronsky, PhD., P.Eng., FCAE

Tag der mündlichen Prüfung: 12. Juli 2019

Fortschritt-Berichte VDI

Reihe 17

Biotechnik/
Medizintechnik

M. Sc. Ben Nikolas Bufe,
Duisburg

Nr. 296

Method for Non-Invasive Skin Artifact-Free Spatial Bone Motion Tracking Using Pressure Sensor Foils

VDI verlag

Bufe, Ben Nikolas
Method for Non-Invasive Skin Artifact-Free Spatial Bone Motion Tracking Using Pressure Sensor Foils
Fortschr.-Ber. VDI Reihe 17 Nr. 296. Düsseldorf: VDI Verlag 2019.
92 Seiten, 53 Bilder, 15 Tabellen.
ISBN 978-3-18-329617-0, ISSN 0178-9600,
€ 38,00/VDI-Mitgliederpreis € 34,50.

Keywords: In-vivo bone motion tracking – Non-invasive – Skin artifact-free – Radiation-free point-model approximation – Pressure-foil palpation – Three-Ellipsoid 2D-3D registration – Pressure point identification

This work addresses the development of a novel method for bone pose estimation that is both, non-invasive and accurate. The main principal is to palpate three prominent bone protuberances using pressure sensor planes attached to the skin. Bone protuberances are approximated by three ellipsoids that are rigidly attached together. The general formulation of the constraint equations is presented and, as a solution approach, an optimization cost function is proposed allowing bone pose tracking that is insensitive toward input errors. The method is validated in-vivo using dual fluoroscopy yielding bone tracking precisions in the submillimeter range and below 1 degree, thus, reaching the same order of magnitude as state of the art model based tracking techniques. Finally, the general approach is extended to automatically approximate the rigid body bone geometry via pressure sensor palpation that allows to fully circumvent radiation exposure, making this approach universally applicable.

Bibliographische Information der Deutschen Bibliothek
Die Deutsche Bibliothek verzeichnet diese Publikation in der Deutschen Nationalbibliographie; detaillierte bibliographische Daten sind im Internet unter www.dnb.de abrufbar.

Bibliographic information published by the Deutsche Bibliothek
(German National Library)
The Deutsche Bibliothek lists this publication in the Deutsche Nationalbibliographie (German National Bibliography); detailed bibliographic data is available via Internet at www.dnb.de.

Von der Fakultät für Ingenieurwissenschaften,
Abteilung Maschinenbau
der Universität Duisburg-Essen
genehmigte Dissertation
Referent: Prof. Dr.-Ing. Andrés Kecskeméthy
Korreferent: Prof. Janet Lenore Ronsky, PhD., P.Eng., FCAE
Datum der mündlichen Prüfung: 12. Juli 2019

Als Manuskript gedruckt. Printed in Germany.
ISSN 0178-9600
ISBN 978-3-18-329617-0

Preface

List of publications

The present thesis was developed as research associate at the Institute of Mechanics and Robotics ("Lehrstuhl für Mechanik und Robotik") at the University of Duisburg-Essen. Many of the contributions and concepts presented in this work were previously published in the following conference publication and proceedings:

- **N. Bufe**, and A. Kecskeméthy. Position analysis of a planar rigid-body tracked by three ellipse pressure points along straight lines. In *Proceedings of the 14th World Congress in Mechanism and Machine Science*, pages 474–482, Taipei, Taiwan, October 25–30 2015.
- **N. Bufe**, A. Heinemann, P. Köhler, and A. Kecskeméthy. An approach for bone pose estimation via three external ellipsoid pressure points. In *15th Int. Symposium on Advances in Robot Kinematics*, Grasse, France, June 27–30 2016.
- **N. Bufe**, G. Kuntze, J. L. Ronsky, and A. Kecskeméthy. Fluoroscopy Validation of Noninvasive 3D Bone-Pose tracking via External Pressure-Foils. In *Proceedings of the ARK 2018 16th International Symposium on Advances in Robot Kinematics*, pages 466–473, Bologna, Italy, July 1–5 2018.

Acknowledgment

First of all, I would like to thank my supervisor Prof. Andrés Kecskeméthy for supporting me throughout my doctoral thesis. I am very grateful that you gave me the opportunity for all the formative discussions that sharpened my critical thinking and that gave me insight into the world of science. I hope that some of your methodical thinking, your skill of dividing a complex problem into its smallest subproblems, and your mastery of communicating research through text and illustrations will remain with me.

The completion of this thesis would not have been possible without our cooperation partners in Canada. First and foremost, I want to thank Prof. Janet Lenore Ronsky for opening the doors to her lab at the University of Calgary. Without her expertise and openness toward this project, the validation of the methods presented that have shaped

this thesis would have been impossible. I would also like to thank her working group, in particular Gregor Kuntze, Payam Zandiyeh, Jessica Küpper and Alonso Figueroa for their valuable contributions and technical assistance. Special thanks go to Sarah Sanni and her family for their incredible hospitality making the stay comfortable and enjoyable.

It has been a privilege to work with many great colleagues that allow for thought-provoking discussions on every aspect of science and life. Not to mention our unforgettable foosball matches after lunch, providing the necessary balance to work.

I also greatly acknowledge the work of my bachelor students I have had the pleasure to work with: Haoming Zhang, Wen Yang, Shenzhi Yang, Oliver Born, Bingxin Shu, Moxi Liang who made meaningful contributions to this thesis.

Finally, I could not be more fortunate to have a family that has always given me unconditional love and support. Without you, I would not be where I am today!

Duisburg, April 2019
Nikolas Bufe

Contents

Notation

In this thesis, general vectors are assumed to be decomposed in the target frame. For other decompositions, the notation ${}^k_i\underline{r}_j$ is used, where i denotes the frame with respect to which the motion is measured, j the target frame and k the frame of decomposition.

Furthermore, ${}^i\mathbf{R}_j$ denotes the rotation matrix transforming coordinates with respect to frame $\mathcal{K}_j$ into coordinates with respect to frame $\mathcal{K}_i$.

Abstract

The knowledge about skeletal kinematics is essential in many biomechanical and medical applications. However, an accurate, non-invasive and radiation-free method for bone motion tracking is still an open issue. This thesis addresses the development of a novel method for bone pose estimation that is both, non-invasive and accurate. The main principal is to palpate three prominent bone protuberances using pressure sensor planes attached to the skin. Bone protuberances are approximated by three ellipsoids that are rigidly attached together.

At first, the geometrical problem of the planar case is analyzed, where ellipsoids become ellipses and sensor planes become lines. After deriving the constraint equations describing the mathematical model of the system, Gröbner bases are used to find the number of possible solutions for two different numerically defined configurations of the lines and the ellipses. As a result, a maximum number of 32 different real solutions for the symmetrical and a maximum number of 64 different complex and real solutions for the general case are obtained. However, using the example of the symmetric case, it can be shown that the solution variety can be significantly reduced. From the 32 real solutions only three solutions are physically plausible, taking into account that pressure points are generated by an ellipse arc facing the lines.

This work also presents the general formulation of the constraint equations for the three dimensional case. As a solution approach, an optimization cost function is proposed including the squared minimal distances between sensors and ellipsoids allowing bone pose tracking that is insensitive toward input errors. Furthermore, a dual fluoroscopy validation of the method for three basic movements of the shank: flexion/extension, abduction/adduction and internal rotation is presented. It is shown that by pressure sensor palpation, bone tracking precisions of 0.5 mm to 1.0 mm and 0.3° to 0.6° can be attained with respect to dual fluoroscopy manual registration, thus, reaching the same order of magnitude as state of the art model based tracking techniques.

Finally, this thesis regards the limiting case where ellipsoids become points allowing the introduction of an automatable procedure approximating the rigid body bone geometry based on data from a previously performed bone pose measurement. Thereby, it is possible to fully circumvent radiation exposure that might be necessary to extract ellipsoid parameters from e. g. a computed tomography scan. Results indicate that deviations to the ellipsoid-approximated bone model are in the submillimeter range and may thus be negligible for many applications.

1 Introduction

1.1 Motivation

Accurate bone motion tracking from external measurements is an important issue in the field of biomechanics, as it is indispensable for patient-specific objective diagnoses. This is why extensive research has been conducted in this field over the past years in order to develop procedures that are primarily accurate but also patient-friendly. Non-invasive procedures for in-vivo studies on bone pose tracking are preferable over intrusive methods to bring the risks of the subject concerned to an absolute minimum. Currently, marker-based motion capture systems are mostly used in clinical practice to determine the kinematics of the skeletal motion of a human body. The concept of those is to estimate bone motion by tracking retro-reflective markers placed on the skin while assuming that they are rigidly attached to the underlying bone. However, the skin moves with respect to the underlying bones during motion, causing an error known as soft tissue artifact that can be up to several centimeters (see Fig. 1.1). In many applications, high accuracy is required to make valid statements about bone kinematics. However, an accurate non-invasive and radiation-free method for bone motion tracking is still an open issue. This thesis presents a novel approach for non-invasive bone motion estimation that was first published 2010 in a patent application by

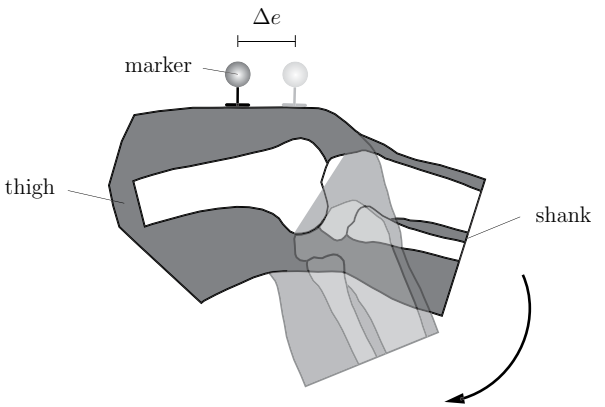

Figure 1.1: Schematic representation of the relative displacement Δe between skin mounted marker and underlying bone during knee flexion from an initial position (dark contours) to an end position (light contours).

Kecskeméthy [37]. In the present work, the right human shank serves as a biological model to describe, establish and validate the mathematical model of this approach. The basic concept is shown in Fig. 1.2. It consists of palpating three prominent bone protuberances with three planar pressure sensor foils, in this case at the following bone landmarks: tuberosity as well as the lateral and medial malleoli. On each sensor, a relative pressure point can be identified representing the closest point to the bone surface under the skin. The contact relevant regions of the palpated bone landmarks can be locally approximated by ellipsoids which are rigidly attached to a body-fixed frame $\mathcal{K}_b$. Moreover, sensor poses are tracked by using a marker-based motion capture system allowing to determine the absolute coordinates of each pressure point. However, while the pressure point coordinates are known, the actual minimal distances between the pressure points and the bone landmarks (representing soft tissue) are unknown. Finally, the geometric problem is to find the possible bone poses $\mathcal{K}_b$ fulfilling these conditions.

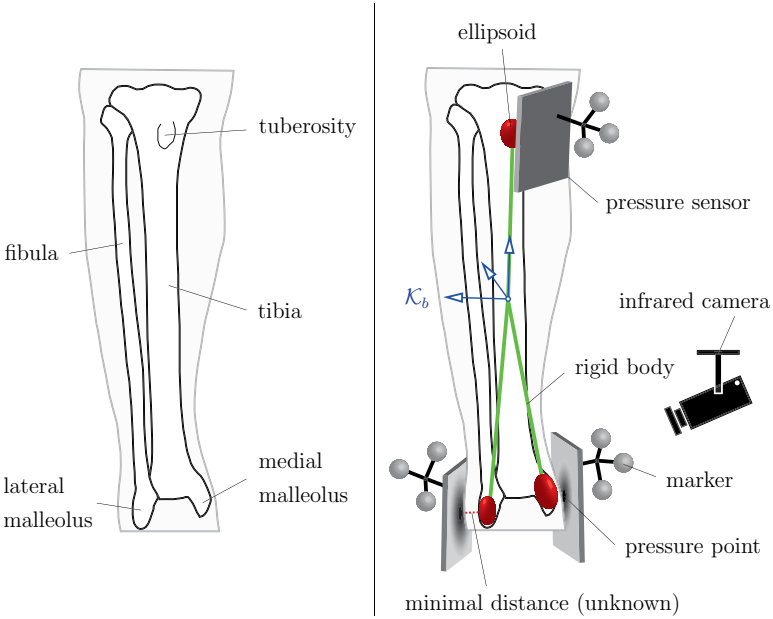

Figure 1.2: Pose detection of the right shank using three pressure points on tracked pressure sensor planes.

Note that in this thesis, ellipsoids were chosen to approximate bone surfaces as they allow different curvatures in two directions. But it will be seen that they can easily be replaced by other conceivable convex surface representations.

The approach takes advantage of the fact that a rigid bone can be sensed under the skin by slightly pressing a pressure sensor on it due to the elasticity of the soft tissue. It is assumed that the palpated pressure distribution primarily originates from the bone structure. This means that the approach is not affected by skin movements and, consequently, is skin artifact-free. Fig. 1.3 shows a distal femur palpated by a sensor foil resulting in a pressure distribution with the highest pressure value located at the point that is closest to the underlying bone. It can be seen that a relative displacement Δe of the sensor foil with respect to the underlying bone results in the same relative displacement Δe of the pressure distribution on the sensor foil. Therefore the absolute position of the pressure distribution remains unchanged and, consequently, is not affected by skin movement.

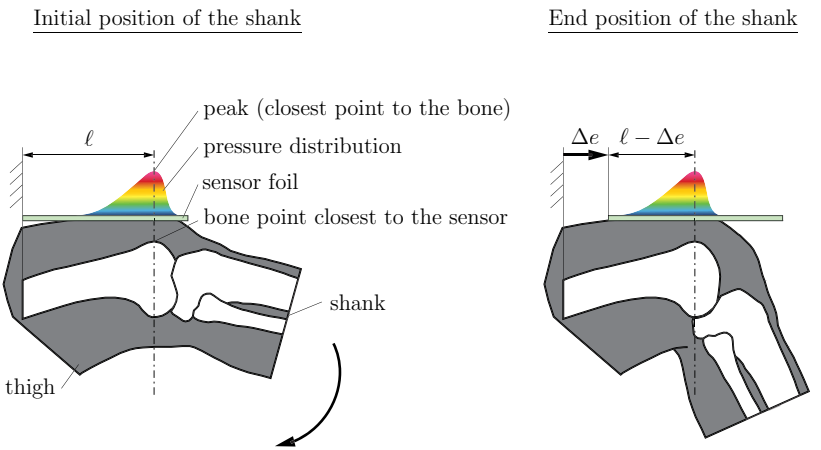

Figure 1.3: Schematic representation of a pressure sensor relatively moved with respect to the underlying bone while the absolute position of the pressure distribution remains unchanged.

1.2 State of the art

To the authors' knowledge, the concept of using pressure sensors to track three dimensional rigid body motion has never been investigated by other working groups yet. For this reason, the following literature research focuses on general procedures for dynamic bone motion tracking.

In the literature, a distinction is made between invasive and non-invasive procedures for bone motion tracking, where non-invasive means that no damage is done to tissue e. g. a cut into the skin. In general, authors agree with the classification of existing procedures with the exception of those based on ionized radiation such as X-rays (authors stating that X-rays are invasive [55, 68] or non-invasive [31, 43]). Note that in this thesis, procedures using X-rays and in particular fluoroscopy will be treated as invasive.

1.2.1 Invasive Procedures

Mainly, two different invasive procedures for dynamic bone motion tracking were investigated in the literature: (1) intra-cortical bone pins and (2) radiation based techniques. The first one mostly published between 1998 to 2004 uses intra-cortical bone pins consisting of metal pins that are inserted into the bone through the soft tissue (see Peters et al. [54]). Multiple retro-reflecting markers are rigidly attached to each metal pin whose spatial position are tracked by infrared cameras. It was shown by Ramsey and Wretenberg that joint motions can accurately be reproduced using bone pins [56]. The accuracy of this procedure mainly depends on the accuracy of the chosen camera system used as well as on parameters such as the number of cameras, the measurement condition (static vs. dynamic), etc. [22, 39, 74]. Older studies reported accuracies in the centimeter range [22, 60] while recent studies using modernized systems were typically in the lower millimeter range or even below 1 mm and 1° [23, 39, 74].

A variant of intra-cortical bone pins are external fixation devices used in surgeries to support broken bones where multiple bone pins are rigidly connected with metal parts [3, 13, 15, 45]. However, Holden et al. and Alexander et al. reported a significant influence of the patients gait due to the presence of external fixation devices (1), as they have the potential to collide with other body segments [34] and (2) because of their additional weight [3, 36].

The use of both, intra-cortical bone pins and external fixation devices, is controversially discussed in the literature. While Ramsey et al. reported that all test persons could

move their leg freely and that no pain was experienced [56], other authors emphasize the risk of avoidable infections, additional pain causing discomfort as well as pin loosening during dynamic measurements making it inappropriate for everyday clinical tests on humans being awake [3, 27, 29, 59, 64]. On the other hand, the use of intra-cortical bone pins is a common practice during surgeries when patients are under anesthesia and thus free of pain [18, 73].

Radiation-based techniques such as fluoroscopy were primarily published since 2005 and are currently considered as gold standard techniques for bone pose tracking [14, 54, 61, 64]. A fluoroscope allows high-frequency image capturing using X-rays to obtain 2D images of inner bone structures. Mainly, two different approaches are used in order to reconstruct bone poses from the fluoroscopic images: (1) Three noncollinear radio-opaque markers are invasively implanted into each bone, whose exact positions with respect to the bone can be derived from e. g. a 3D computed tomography (CT) scan, enabling 6-degrees of freedom motion tracking (marker-based technique). (2) A 3D CT bone model of each bone is either manually or automatically registered to the fluoroscopic images to obtain the associated translations and rotations (markerless or model based registration technique). Older studies using only one fluoroscope (also referred to as single-plane fluoroscopy) reported in-plane accuracies in the submillimeter range in translation but out-of-plane errors of at least one order of magnitude higher [6, 26, 30]. The simultaneous use of two differently positioned fluoroscopes is called biplane fluoroscopy or dual fluoroscopy, creating a stereoscopic view of the bones allowing 3D skeletal kinematics analysis [49, 64]. Anderst et al. and Tashman et al. have shown that dual fluoroscopic implanted marker tracking for dynamic bone motions is very precise with 70-120 μm [5, 67]. This is why it is also used as gold standard method to validate model based techniques achieving deviations below 1 mm and 1° [5].

However, Masum et al. note that marker-based fluoroscopy can only be applied in post-operative studies owing to the need of invasive marker implantation [47]. Furthermore, it was criticized by Karlsson and Tranberg that human exposure to ionizing radiation should be avoided as much as possible as it may increase the risk of cancer, thus limiting measurements to a minimal number of exposures per second, or even making them completely unacceptable for ethics committees [36]. The same authors also mention the small field of view of fluoroscopic systems restricting experiments to local areas and specific movement patterns.

1.2.2 Non-invasive Procedures

Marker-based motion capture systems for e. g. patient-specific objective diagnoses are the most popular non-invasive approach for medical applications and are considered to be the gold standard for non-invasive bone motion tracking [16]. The main principle of this procedure is to determine the trajectory of retro-reflecting markers attached to the skin using infrared cameras, assuming that they represent the motion of the underlying bone segments. However, during dynamic measurements, it is known that markers suffer from soft tissue artifacts (STA), that is relative displacements between skin marker and bone. It is described in the literature that STAs can become considerably large being a matter of several centimeters. It depends on the marker location as well as the body segments motion pattern [2, 64] which is why STAs are considered to be the most critical source of error in movement analysis [15].

In order to compensate STAs, different approaches have been investigated, which were mostly compared to intra-cortical bone pins or fluoroscopy (see Section **1.2.1**). Instead of using single markers, the use of marker sets or marker clusters could reduce errors due to skin movement by several millimeters [3, 13, 45]. Alexander et al. showed that skin deformations during dynamic motion can be classified into a systematic error depending on the movement pattern performed and a statistical error that can be compensated by applying Gaussian noise filter techniques [3]. This reduced STA errors by one third. According to Fuller et al. [27] it is very complex to determine the definition of corrective transformations between marker and bone to eliminate systematic errors due to the task dependent behavior. Therefore, he concludes that this approach is very time-consuming for cyclic and not appropriate for general movement patterns. Holden et al. observed differences in skin displacement patterns that are even both, task and subject dependent [34]. This may be the reason why Peters et al. state that despite the fact that "these more recent techniques have led to advances in STA research, they have not always been accompanied by changes in clinical practice" [54].

Lu and O'Connor firstly introduced global optimization techniques, describing the human body as a multi-link musculoskeletal model where individual links are connected by joint constraints [44]. The 3D pose of the model can be determined by minimizing the distances between measured and model based marker positions reducing STA errors by up to 60% [58]. However, the reliability of global optimization techniques is controversially discussed, because according to Andersen et al. the error introduced by the joint constraints have the same order of magnitude than errors due to STA [4]. A study by Stagni et al. reported deviations of 10° and 10-15 mm for joint rotations and

translations between multiple repetitions of the same movement pattern, questioning its effectiveness over marker cluster techniques where deviations of 1-2° and 1-3 mm were obtained [63].

Recent studies proposed the use of ultrasound transducers at different anatomical locations in order to obtain either coordinates of discrete points or curves of the underlying bone surface [35, 47]. Absolute coordinates of the points were identified by combining the ultrasound with a marker-based motion capture system. Subsequently, a 3D model of the bone surface from a CT/MRI (magnetic resonance imaging) scan was used which was fitted into the point cloud by optimization. Niu et al. showed that a maximum measured root mean square error of 3.44° and 4.88 mm could be achieved compared to intra-cortical bone pins for dynamic in-vivo tibiofemoral measurements, or even better in a cadaveric study [51, 52].

In addition to the non-invasive procedures specified above, other measurement techniques were used in order to track bone motions such as MRI [54], inertial measurement units (IMUs) [25, 46, 53, 69, 66], or other optical markerless motion capture systems e. g. Microsoft Kinect [10, 20, 24, 28]. However, they will not be taken into further consideration here because either they allow only static measurements (MRI), or they are equally affected by STA but with a lower overall accuracy as marker-based motion capture systems (IMU, Kinect, etc.).

1.3 Objective and overview

The objective of this thesis is to develop a novel bone pose estimation method that is both non-invasive and accurate. This includes a complete description of the mathematical model and its solution variety of the planar case in order to clarify the solvability of the system and its sensitivity. The extension of the mathematical formulas to 3D should provide the possibility to measure bone poses in a real application. In this context, an automatable procedure is proposed allowing approximation of the bone geometry without knowledge of its real dimensions e. g. by means of a computed tomography scan in order to fully circumvent radiation exposure. As a major part, the present work aims to test the hypothesis that bone poses can be determined with high accuracy.

The work is organized as follows: Chapter **2** analyzes the planar case of the bone pose reconstruction procedure presented in this thesis. The composition of the 2D

model is described in detail as well as the derivation of the mathematical model. The solution variety of the established constraint equations is further investigated using Gröbner bases. The chapter closes with a suggestion of how the insight of the resulting solutions can be used in order to significantly reduce the solution variety.

Chapter **3** extends the mathematical model of Chapter **2** to the general three dimensional case. An optimization cost function is proposed that allows a numerically robust solution finding of the constraint equations as shown in a subsequent sensitivity analysis.

Then, Chapter **4** deals with the limiting case where all contact relevant bone regions are approximated by points instead of ellipsoids. This is followed by the introduction of an automatable procedure that approximates the rigid body geometry based on data from a previously performed bone pose measurement.

Chapter **5** addresses the validation of the previously introduced method for bone pose determination. It includes the validation of the pressure point identification from a given pressure distribution. Furthermore, the ellipsoid- as well as the point-approximated bone model introduced in the preceding chapters are validated using a dual fluoroscopy system.

Chapter **6** summarizes the major findings of this thesis and provides an outlook for future work.

2 Geometrical problem analysis for the planar case

In this chapter, the position analysis of a rigid body comprising three ellipses for which the pressure points are tracked along straight lines is discussed. This corresponds to the planar case of the bone pose reconstruction procedure presented in this thesis. First, the 2D model is described in detail. After deriving the constraint equations describing the mathematical model of the system, Gröbner bases are used to find the number of possible solutions for two different numerically defined configurations of the lines and the ellipses. Finally, it is shown how the insight of the resulting solutions can be used in order to significantly reduce the solution variety. Those results are crucial for subsequent bone motion reconstruction in 3D ensuring a numerically robust computation of the bone pose.

2.1 2D model description

In the planar case, the ellipsoids become ellipses and the pressure sensor foils become lines (Fig. 2.1). Assuming that the pressure points of three bone landmarks are tracked, and that three lines as well as distances s_i along those lines of the pressure points are given, the question is which poses of the rigid body pose $\mathcal{K}_b$ may be recovered from the given measurements. Note that, as the compression of the soft tissue between pressure foils and bone landmarks is unknown, the minimal distance d_i along the common normal of pressure line and bone landmark profile is a dependent, unknown variable.

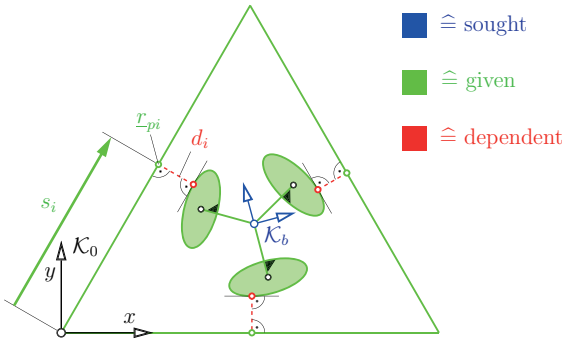

Figure 2.1: 2D pose detection of a rigid body using pressure point tracking along given lines.

The problem is similar to the 3PPR planar parallel manipulator analyzed by Choi [19] (Fig. 2.2): If one substitutes the ellipses by circles, then the pressure point becomes the input motion $\hat{s}_i$ along the side tracks, and the tangent is taken with respect to the proximal and distal points on the circumference of the revolute joints of the platform. While it was shown by Choi that the 3PPR manipulator always has two solutions, it will be seen that the pose detection of a rigid body for which three pressure points of ellipses are prescribed, as shown in Fig. 2.1, leads to a larger set of solutions.

In this thesis, a setup of a symmetric system shown in Fig. 2.1 is analyzed first, where both the three lines and the three centers of the ellipses form equilateral triangles. Additionally, all three ellipses are oriented such that the extensions of their minor axes intersect at the geometric center of the triangle formed by the centers of the ellipses. However, the constraint equations derived in Section **2.2** will describe a general configuration of the system.

As is the case for the 3PPR planar manipulator, the analyzed system provides three-degree-of-freedom motions, i. e. two translations and one rotation in the plane, where the distances s_i along the lines define the input variables.

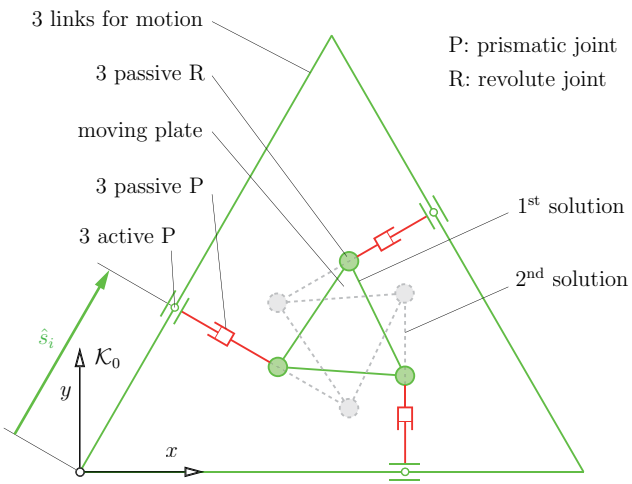

Figure 2.2: Sample configuration of a 3PPR parallel manipulator with its two possible solutions (see [19]).

2.2 Formulation of the constraint equations

In this section, the constraint equations of the general system shown in Fig. 2.3 are derived. For simplicity, all three lines and ellipses are summarized in one equation set using the index $i = 1, \ldots, 3$, as the general structure of the equations relating the pressure point to the corresponding tangent point on the ellipse are the same for all three ellipses.

Let $\underline{r}_{ci}$ be the center of the ellipse $\underline{\mathcal{E}}_i$ and $\mathbf{A}_i$ be the 2×2 diagonal matrix so that

$$\mathbf{A}_i = \begin{bmatrix} \dfrac{1}{a_i^2} & 0 \\ 0 & \dfrac{1}{b_i^2} \end{bmatrix} , \tag{2.1}$$

with its semi-major axis a_i and the semi-minor axis b_i. Then, the matrix representation of the equation of an ellipse whose major and minor axes coincide with the Cartesian axes is

$$(\underline{r}_{ti} - \underline{r}_{ci})^{\mathrm{T}} \, \mathbf{A}_i \, (\underline{r}_{ti} - \underline{r}_{ci}) - 1 = 0 \, , \tag{2.2}$$

where $\underline{r}_{ti}$ denotes an arbitrary point on the surface of the ellipse $\underline{\mathcal{E}}_i$. As can be seen in Fig. 2.3, each ellipse is rotated with respect to the inertial system by a sequence of two rotations: (1) a rotation $\mathbf{R}$ of the rigid body frame $\mathcal{K}_b$ with respect to the inertial frame $\mathcal{K}_0$, followed by (2) a rotation $\mathbf{R}_i$ of ellipse $\underline{\mathcal{E}}_i$ with respect to the rigid body frame, where

$$\mathbf{R} = \begin{bmatrix} \cos\varphi_b & -\sin\varphi_b \\ \sin\varphi_b & \cos\varphi_b \end{bmatrix} , \; \mathbf{R}_i = \begin{bmatrix} \cos\alpha_i & -\sin\alpha_i \\ \sin\alpha_i & \cos\alpha_i \end{bmatrix} . \tag{2.3}$$

This leads to the first constraint equation describing a general rotated ellipse $\underline{\mathcal{E}}_i$

$$(\underline{r}_{ti} - \underline{r}_{ci})^{\mathrm{T}} \, \mathbf{R} \, \mathbf{R}_i \, \mathbf{A}_i \, (\mathbf{R} \, \mathbf{R}_i)^{\mathrm{T}} \, (\underline{r}_{ti} - \underline{r}_{ci}) - 1 = 0 \, . \tag{2.4}$$

The ellipse centers can be described as

$$\underline{r}_{ci} = \underline{r}_b + \mathbf{R} \, \Delta\bar{\underline{r}}_i \, , \tag{2.5}$$

where $\underline{r}_b = [x_b, y_b]^{\mathrm{T}}$ are the coordinates of the rigid body center and $\Delta\bar{\underline{r}}_i$ is the vector from the rigid body center to the ellipse center in body-fixed coordinates.

Furthermore, the gradient of the ellipse $\underline{\mathcal{E}}_i$ at point $\underline{r}_{ti}$ is

$$\operatorname{grad} \underline{\mathcal{E}}_i = \mathbf{R} \, \mathbf{R}_i \, \mathbf{A}_i \, (\mathbf{R} \, \mathbf{R}_i)^{\mathrm{T}} \, (\underline{r}_{ti} - \underline{r}_{ci}) \tag{2.6}$$

and should be parallel to the normal vector $\underline{n}_{\mathcal{T}_i}$ of line $\mathcal{T}_i$ in order to ensure that the tangent at point $\underline{r}_{ti}$ is parallel to the line $\mathcal{T}_i$. This leads to the second constraint

$$\mathbf{R}\,\mathbf{R}_i\,\mathbf{A}_i\,(\mathbf{R}\,\mathbf{R}_i)^{\mathrm{T}}\,(\underline{r}_{ti}-\underline{r}_{ci})-\lambda_i\,\underline{n}_{\mathcal{T}_i}=\underline{0}\,, \tag{2.7}$$

where λ_i is an arbitrary scalar.

Finally, let $\underline{r}_{pi}$ be the radius vector to the given pressure point on the line $\mathcal{T}_i$. The difference vector of the two points $\underline{r}_{pi}$ and $\underline{r}_{ti}$ has to be normal to the line $\mathcal{T}_i$. The corresponding constraint equation can thus be stated as

$$(\underline{r}_{ti}-\underline{r}_{pi})^{\mathrm{T}}\,\underline{u}_{\mathcal{T}_i}=0\,, \tag{2.8}$$

whereas $\underline{u}_{\mathcal{T}_i}$ denotes the direction vector of the line $\mathcal{T}_i$.

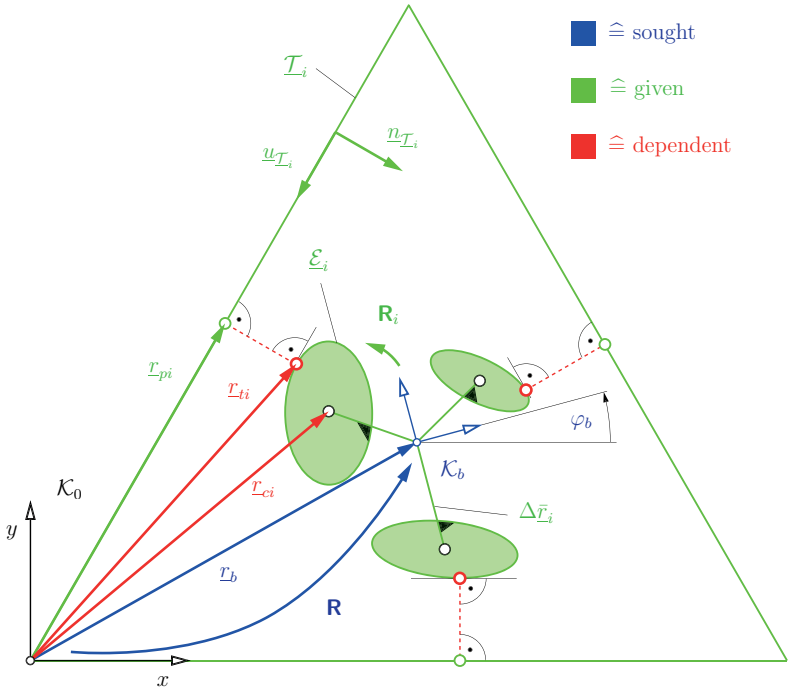

Figure 2.3: Description of the mathematical model for a general configuration of the rigid body.

2.3 Characteristics of a symmetric configuration

It can be concluded ad hoc that solutions of a symmetric configuration must always occur in pairs. A pair consists of two solutions with the same position (x_b, y_b) but different orientations φ_b of the rigid body frame $\mathcal{K}_b$ (Fig. 2.4).

Given a pressure point $\underline{r}_{pi}$ on the line $\underline{\mathcal{T}}_i$ with its normal vector $\underline{n}_{\underline{\mathcal{T}}_i}$, we suppose that $\mathcal{K}_b$ is a possible solution for the pose of the rigid body center for a symmetric configuration with its position $\underline{r}_b = [x_b, y_b]^{\mathrm{T}}$ and orientation $\mathbf{R} = \mathtt{Rot}\,[\,z, \varphi_b\,]$. In addition, the dependent variable $\underline{r}_{ti}$ defines the specific point on the surface of the ellipse which is tangential to the line $\underline{\mathcal{T}}_i$, which can be expressed as

$$\underline{r}_{ti} = \underline{r}_{ci} + {}_{ci}\underline{r}_{ti} \tag{2.9}$$

$$\underline{r}_{ti} = \underline{r}_{ci} + \mathbf{R}\,\mathbf{R}_i\,\mathbf{R}_{\beta_i} \begin{bmatrix} \ell_i \\ 0 \end{bmatrix}, \tag{2.10}$$

whereas $\mathbf{R}_{\beta_i} = \mathtt{Rot}\,[\,z, \beta_i\,]$ defines the rotation of the vector ${}_{ci}\underline{r}_{ti}$ from the ellipse center $\underline{r}_{ci}$ to the point $\underline{r}_{ti}$ with respect to $\mathcal{K}_{\underline{\mathcal{E}}_i}$, and ℓ_i shall be the length of ${}_{ci}\underline{r}_{ti}$.

For any symmetric configuration, there must be a second solution $\mathcal{K}'_b$ for the pose of the rigid body frame, with the same position $\underline{r}_b$ but mirrored about the line $\underline{\mathcal{S}}_i$ which is parallel to the line $\underline{\mathcal{T}}_i$ such that

$$\varphi'_b = -(\varphi_b + 2\alpha_i) \qquad \text{and} \qquad \beta'_i = -\beta_i\,. \tag{2.11}$$

Thus, the rotation matrices of the second solution can be described by

$$\mathbf{R}' = \mathtt{Rot}\,[\,z, \varphi'_b\,] \qquad \text{and} \qquad \mathbf{R}'_{\beta_i} = \mathtt{Rot}\,[\,z, \beta'_i\,], \tag{2.12}$$

while $\mathbf{R}'_i = \mathbf{R}_i$ remains unchanged. By solving the constraint Eqs. (2.4), (2.7) and (2.8) symbolically with *MAPLE*, it follows that

$$\underline{\mathcal{E}}_i(\underline{r}_{ti}) - \underline{\mathcal{E}}'_i(\underline{r}'_{ti}) = 0 \tag{2.13}$$

$$\mathrm{grad}\ \underline{\mathcal{E}}_i(\underline{r}_{ti}) - \mathrm{grad}\ \underline{\mathcal{E}}'_i(\underline{r}'_{ti}) - \lambda_i\,\underline{n}_{\underline{\mathcal{T}}_i} = \underline{0} \tag{2.14}$$

$$(\underline{r}_{ti} - \underline{r}'_{ti})^{\mathrm{T}}\,\underline{u}_{\underline{\mathcal{T}}_i} = 0 \tag{2.15}$$

with the scalar

$$\lambda_i = \ell_i \sin(\varphi_b + \alpha_i + \beta_i) \left(\frac{1}{a_i^2} + \frac{1}{b_i^2}\right) + \ell_i \sin(\varphi_b + \alpha_i - \beta_i) \left(\frac{1}{a_i^2} - \frac{1}{b_i^2}\right). \tag{2.16}$$

It can therefore be stated that a second solution with the same position $\underline{r}_b$ exists that is fulfilling the constraint equations.

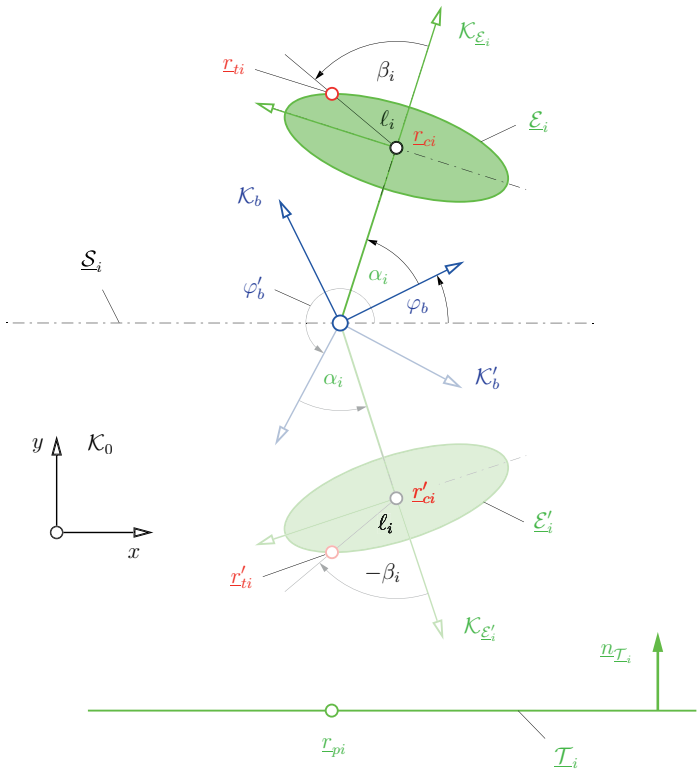

Figure 2.4: A sample solution pair of a symmetric case demonstrated by means of one ellipse.

2.4 Determination of the solution variety using Gröbner bases

2.4.1 Gröbner bases

Gröbner bases are very wide-ranging in scope. This section will focus on using the method of computing a suitable Gröbner basis to face the problem of computationally solving multivariate polynomial equations.

A polynomial is a finite sum of monomials comprising variables with nonnegative integer exponents and a coefficient. In general, determining the algebraic variety of a set of polynomials is not trivial. However, this task can sometimes be achieved by com-

puting a Gröbner basis, an equivalent set of polynomials having the same algebraic variety but composed of other polynomials with certain properties that allow simple algorithmic solutions. In order to systematically compute a Gröbner basis from a set of polynomials, division algorithms such as the *Buchberger's Algorithm* are used (see e. g. the book by Cox et al. [21] for more information about division algorithms).

The operations of a division algorithm and thus the resulting Gröbner basis depend on the choice of how the polynomial terms are initially ordered, called monomial order. Different monomial orderings exist, each leading to different Gröbner bases. A common ordering is called *lexicographic ordering* (other designations are *lex* or *PLEX* for "pure lexicographic order"), where variables are ordered alphabetically, thus, analogously to the ordering of words in dictionaries. For example, on $\mathbb{C}[x, y]$ lexicographic ordering means

$$1 \prec y \prec y^2 \prec \cdots \prec x \prec xy \prec xy^2 \prec \cdots x^2 \prec x^2y \prec x^2y^2 \prec \cdots .$$

Here, lexicographic ordering is of interest as it allows the basic strategy of elimination theory (see [21]). Thereby, the derived constraint Eqs. (2.4), (2.7) and (2.8) are transformed into a new set of equations with the same algebraic variety but in triangular form (i. e. the first equation is only dependent on the first variable, the second equation is only dependent on the first and the second variable, etc.). Once this goal is achieved, univariate root-finding algorithms can be applied to the first equation. Back-substituting the solutions into the second equation leads to an equation which is again only dependent on one variable. Provided that the Gröbner basis with lexicographic ordering can be computed, the solution variety can thus be found.

2.4.2 Application examples

In order to find all possible solutions of the constraint Eqs. (2.4), (2.7) and (2.8), Gröbner bases with respect to lexicographic monomial ordering were used to eliminate all intermediate variables, such as λ_i. A reduced system of polynomial equations is generated in terms of the three unknown pose variables (x_b, y_b, φ_b) of the rigid body frame $\mathcal{K}_b$. At first, to compute Gröbner bases, it is necessary to transform the constraint equations into a system of polynomial equations. This was achieved after introducing the auxiliary variables

$$s = \sin\varphi_b\,, \qquad c = \cos\varphi_b \tag{2.17}$$

Table 2.1: Parameters of the symmetric configuration analyzed in this thesis (lengths are given in unit length).

Index	Rigid body parameters				Line parameters	
i	a_i	b_i	α_i	$\Delta\underline{\bar{r}}_i$	$\underline{n}_{\underline{\mathcal{T}}_i}$	$\underline{r}_{pi}$
1	4	1	$\frac{\pi}{3}$	$\begin{bmatrix} -3\frac{\sqrt{3}}{2} \\ \frac{3}{2} \end{bmatrix}$	$\begin{bmatrix} \frac{\sqrt{3}}{2} \\ -\frac{1}{2} \end{bmatrix}$	$\begin{bmatrix} 5-5\frac{\sqrt{3}}{2} \\ \frac{15}{2} \end{bmatrix}$
2	4	1	0	$\begin{bmatrix} 0 \\ -3 \end{bmatrix}$	$\begin{bmatrix} 0 \\ 1 \end{bmatrix}$	$\begin{bmatrix} \frac{11}{2} \\ 0 \end{bmatrix}$
3	4	1	$-\frac{\pi}{3}$	$\begin{bmatrix} 3\frac{\sqrt{3}}{2} \\ \frac{3}{2} \end{bmatrix}$	$\begin{bmatrix} \frac{\sqrt{3}}{2} \\ \frac{1}{2} \end{bmatrix}$	$\begin{bmatrix} 5+5\frac{\sqrt{3}}{2} \\ \frac{15}{2} \end{bmatrix}$

for the trigonometric functions. The additional constraint

$$s^2 + c^2 - 1 = 0 \tag{2.18}$$

was added to the system of equation to ensure that the variables s and c are on the unit circle.

The resulting general system of polynomial equations f_k with $k = 1, \ldots, 13$ can be summarized as follows

$$\begin{aligned}
f_{1\text{-}3}&: \quad (\underline{r}_{ti} - \underline{r}_{ci})^{\mathrm{T}}\, \mathbf{R}\,\mathbf{R}_i\,\mathbf{A}_i\,(\mathbf{R}\,\mathbf{R}_i)^{\mathrm{T}}\,(\underline{r}_{ti} - \underline{r}_{ci}) - 1 = 0 \\
f_{4\text{-}9}&: \quad \mathbf{R}\,\mathbf{R}_i\,\mathbf{A}_i\,(\mathbf{R}\,\mathbf{R}_i)^{\mathrm{T}}\,(\underline{r}_{ti} - \underline{r}_{ci}) - \lambda_i\,\underline{n}_{\underline{\mathcal{T}}_i} = 0 \\
f_{10\text{-}12}&: \quad (\underline{r}_{ti} - \underline{r}_{pi})^{\mathrm{T}}\,\underline{u}_{\underline{\mathcal{T}}_i} = 0 \\
f_{13}&: \quad s^2 + c^2 - 1 = 0\ ,
\end{aligned}$$

with index $i = 1, \ldots, 3$. Using the `Groebner` library of *MAPLE* [50], Gröbner bases of the system

$$\underline{F} = (f_1, \ldots, f_{13}) \tag{2.19}$$

could be computed for numerical values of the polynomial coefficients. Thus, in the present context, the numeric values displayed in Table 2.1 were used to present in more detail a sample configuration of a symmetric case. Hereby, the point $\underline{r}_{pi}$ was also used as support vector for the line $\underline{\mathcal{T}}_i$.

In particular, for the computation of the Gröbner basis of the system $\underline{F}$, the `Groebner` library and the `PolynomialIdeals` library of *MAPLE* [50] were used. *MAPLE* requires the term order as well as a list of variables to determine how the variables are ordered.

Table 2.2: Parameters of the general configuration analyzed in this thesis (lengths are given in unit length).

Index	Rigid body parameters				Line parameters	
i	a_i	b_i	α_i	$\Delta\underline{\bar{r}}_i$	$\underline{n}_{\mathcal{T}_i}$	$\underline{r}_{pi}$
1	2	1	$\frac{7\pi}{20}$	$\begin{bmatrix} -3\frac{\sqrt{3}}{2} \\ \frac{3}{2} \end{bmatrix}$	$\begin{bmatrix} \frac{\sqrt{2}}{2} \\ \frac{\sqrt{2}}{2} \end{bmatrix}$	$\begin{bmatrix} -3 \\ 2 \end{bmatrix}$
2	8	1	$\frac{\pi}{36}$	$\begin{bmatrix} 0 \\ -3 \end{bmatrix}$	$\begin{bmatrix} 0 \\ 1 \end{bmatrix}$	$\begin{bmatrix} 5 \\ 0 \end{bmatrix}$
3	$\frac{81}{10}$	1	$-\frac{11\pi}{60}$	$\begin{bmatrix} 3\frac{\sqrt{3}}{2} \\ \frac{3}{2} \end{bmatrix}$	$\begin{bmatrix} -\frac{\sqrt{3}}{2} \\ \frac{1}{2} \end{bmatrix}$	$\begin{bmatrix} 14 \\ 5 \end{bmatrix}$

In the case of lexicographic order *PLEX* with variables $y_b \prec x_b \prec c \prec s$, *MAPLE* found the following Gröbner basis:

$$\begin{aligned}
g_1 &= 74649600s^8 - 10108800s^7 - 51682320s^6 + 3819960s^5 + 4411521s^4 \\
&\quad + 298512s^3 - 7026s^2 - 72s + 1 && (2.20)\\
g_2 &= c^2 + s^2 - 1 && (2.21)\\
g_3 &= 17280s^4x_b - 92160s^4 - 1620s^3x_b + 8640s^3 - 1683s^2x_b + 8976s^2 \\
&\quad - 108sx_b + 576s + 3x_b - 16 && (2.22)\\
g_4 &= -4976640s^6 + 673920s^5 + 3777264s^4 - 299592s^3 - 490623s^2 \\
&\quad + 13824sx_b + 2304x_b^2 - 75960s - 25344x_b + 69695 && (2.23)\\
g_5 &= 5760s^4y_b - 28800s^4 - 540s^3y_b + 2700s^3 - 561s^2y_b + 2805s^2 \\
&\quad - 36sy_b + 180s + y_b - 5 && (2.24)\\
g_6 &= -6sy_b + x_by_b + 30s - 5x_b - 5y_b + 25 && (2.25)\\
g_7 &= -4976640s^6 + 673920s^5 + 3777264s^4 - 299592s^3 - 490623s^2 \\
&\quad - 13824sx_b + 2304y_b^2 + 71496s + 768x_b - 23040y_b + 53567\,. && (2.26)
\end{aligned}$$

In order to find the corresponding solutions of the system $\underline{G} = (g_1, \ldots, g_7)$, the explicit solver of *MAPLE* was used.

General cases have also been regarded to analyze the differences to the symmetric architecture. A sample set of parameters for the general configuration analyzed here is summarized in Table 2.2.

For the symmetric architecture, a maximum number of 32 different real solutions in 16

Table 2.3: Numerical solutions for each pair of the symmetric case shown in Fig. 2.5 and Fig. 2.6.

Pair	x_b	y_b	$\varphi_{b,\text{dark}}$ [deg]	$\varphi_{b,\text{light}}$ [deg]	Pair	x_b	y_b	$\varphi_{b,\text{dark}}$ [deg]	$\varphi_{b,\text{light}}$ [deg]
(a)	1.37	5.00	22.67	157.33	(i)	5.13	4.64	178.80	1.20
(b)	3.74	2.24	-12.11	-167.89	(j)	5.33	5.00	179.47	0.53
(c)	4.38	3.35	-174.10	-5.90	(k)	4.38	6.65	-5.90	-174.10
(d)	5.33	5.00	52.86	127.14	(l)	3.74	7.76	-12.11	-167.89
(e)	5.33	5.00	-48.66	-131.34	(m)	5.75	5.00	178.80	1.20
(f)	5.13	5.36	178.80	1.20	(n)	8.52	5.00	-167.89	-12.11
(g)	5.33	5.00	-0.80	-179.20	(o)	7.31	8.43	157.33	22.67
(h)	7.23	5.00	-174.10	-5.90	(p)	7.31	1.57	157.33	22.67

pairs were found. Fig. 2.5 and Fig. 2.6 show all 16 pairs for the example configuration stated in Table 2.1. For each solution, the contact point on the line and its corresponding point on the ellipse are marked with a different marker for each line. The corresponding numerical solutions are given in Table 2.3. Note that the solutions are genuinely different, i. e. they do not result from each other by cyclic transformations, as the pressure point of each line is only associated to one unique ellipse.

For a general configuration, a maximum number of 64 solutions were found, whereas the maximum number of real solutions found so far was 48. The general set of parameters

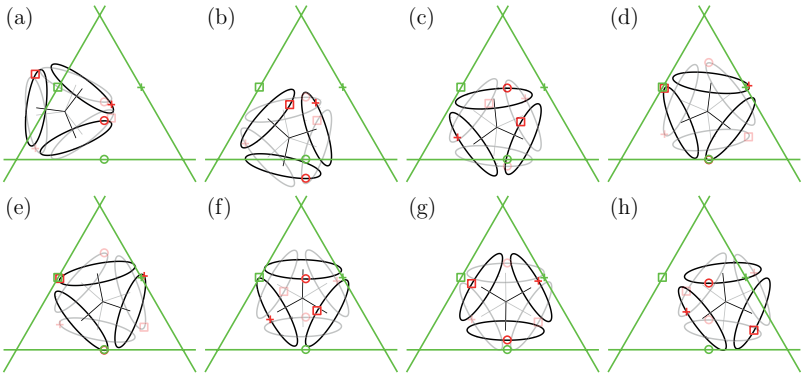

Figure 2.5: The first 8 pairs for the symmetric case of a total of 16 pairs of real solutions (dark color and light color, respectively) with equal center points.

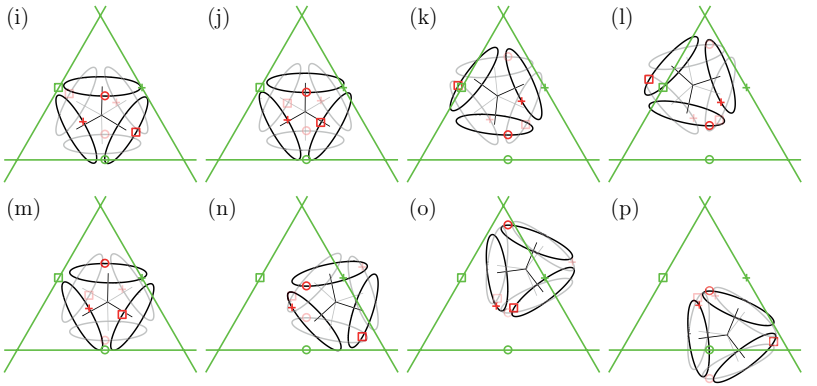

Figure 2.6: The last 8 pairs for the symmetric case of a total of 16 pairs of real solutions (dark color and light color, respectively) with equal center points.

given in Table 2.2 represents one example where 48 different poses for the rigid body frame $\mathcal{K}_b$ exist (Fig. A.1.1 and Fig. A.1.2, Appendix). The corresponding numerical solutions are given in Table A.1.1 in the Appendix. Note that no pairs exist for the general configuration.

2.4.3 Sensitivity analysis

The effect of a small variation of the input variables on the output can be verified by variating the coordinates of the pressure point $\underline{r}_{p2}$ by a small amount, e. g. $\Delta e = 0.001$. One obtains for example

$$\underline{r}_{p2} = \begin{bmatrix} \frac{11}{2} + \Delta e \\ 0 \end{bmatrix} = \begin{bmatrix} \frac{11}{2} + \frac{1}{1000} \\ 0 \end{bmatrix}. \tag{2.27}$$

Table 2.4 summarizes the deviations between the new solutions compared to the original data of Table 2.1. It can be seen that small deviations on the input variables also produce small deviations on the output in the same range.

2.4.4 Reduction of the solution variety

The results show that a maximum number of 32 solutions for the symmetric and a maximum number of 64 solutions for the general case exist. As already indicated,

Table 2.4: Deviation of the rigid body pose for small variations of the input variables.

Pair	Δx_b 10^{-3}	Δy_b 10^{-3}	$\Delta\varphi_{b,\mathrm{dark}} = \Delta\varphi_{b,\mathrm{light}}$ 10^{-4}[rad]	Pair	Δx_b 10^{-3}	Δy_b 10^{-3}	$\Delta\varphi_{b,\mathrm{dark}} = \Delta\varphi_{b,\mathrm{light}}$ 10^{-4}[rad]
(a)	0.49	0.00	1.36	(i)	0.25	0.72	0.42
(b)	2.26	2.76	3.85	(j)	0.67	0.00	0.19
(c)	2.14	4.86	3.58	(k)	2.14	4.86	3.58
(d)	0.67	0.00	0.73	(l)	2.26	2.76	3.85
(e)	0.67	0.00	0.74	(m)	1.50	0.00	0.42
(f)	0.25	0.72	0.42	(n)	2.52	0.00	3.85
(g)	0.67	0.00	0.28	(o)	0.75	0.15	1.36
(h)	0.63	0.00	3.58	(p)	0.75	0.15	1.36

Gröbner bases for this system could only be computed when the polynomial coefficients are given in the form of numerical values. Consequently, the results cannot be generalized with certainty, as only a finite set of parameters have yet been checked. Of course, special geometries can lead to smaller numbers of solutions. For example, in the case of a general system for which all three ellipses are transformed into circles, so that $a_i = b_i$, exactly two different poses of the rigid body are found. This is consistent with the analytical results of Choi [19]. As an exception, it can be easily seen that an infinite number of solutions exist if all the three lines are parallel to each other.

Furthermore, by comparing the pose of a set of solutions, it can be seen that solutions can be very close to each other, which can lead to poorly conditioned numerical behavior. Table 2.5 shows several comparisons between two different solutions of the symmetric configuration of Table 2.1. The distance $\Delta\underline{r}$ between two different solutions, as well as the deviation $\Delta\underline{\varphi}$ of the rotation angles are illustrated. In order to be able to compare the total deviation between two solutions, the variable Δs is introduced such that

$$\Delta s = \|\Delta\underline{r}\| + \kappa \cdot \|\Delta\underline{\varphi}\|\,, \tag{2.28}$$

whereas κ is a characteristic length [57], specifying here the maximum length between two ellipse centers, i. e. for the symmetric case $\kappa = 3\sqrt{3}$. As 32 solutions exist overall, $\binom{32}{2} = 496$ different comparisons can be made, which are sorted by ascending numbers of Δs in Table 2.5.

Table 2.5: Several comparisons between different solutions of the symmetric case shown in Fig. 2.5 and Fig. 2.6.

Case	Solutions			Deviations	
i	j	k	Δs_i	$\|\Delta \underline{r}_i\|$	$\|\Delta \underline{\varphi}_i\|$ [deg]
1	23	26	0.1205	0.0000	1.3282
2	7	10	0.1205	0.0000	1.3282
3	23	27	0.4765	0.4161	0.6655
⋮	⋮	⋮	⋮	⋮	⋮
496	2	32	24.7504	7.1423	169.4343

Considering the present application, i. e. the reconstruction of the bone motion with pressure sensors, only three different solutions are physically meaningful (Fig. 2.7), as the ellipse contact point must face the corresponding line. In addition to that, it can be seen that the total deviations Δs_i of all three solutions are considerably large (Table 2.6). This property can be used to avoid rigid body pose "jumps" between different solutions in numerical computations. The results are of interest for the problem of determining the 3D pose of a bone from measurements of bone landmarks by pressure sensors, which is to be tackled in the next chapter.

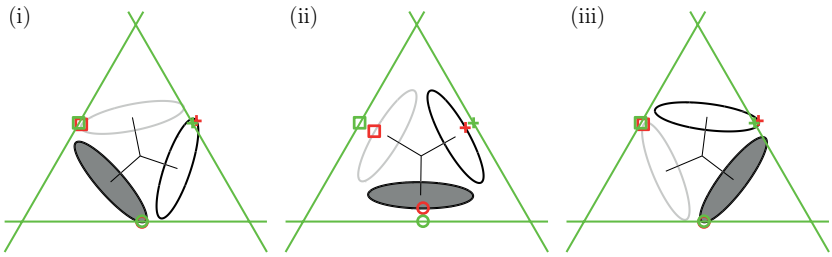

Figure 2.7: The only three solutions of the symmetric configuration where each ellipse tangent point is facing the straight line.

Table 2.6: Comparison between the three solutions of Fig. 2.7.

Case (Fig. 2.7)	Solutions		Deviations		
i	j	k	Δs_i	$\|\Delta \underline{r}_i\|$	$\|\Delta \underline{\varphi}_i\|$ [deg]
(i)	(i)	(ii)	4.96	0.00	47.86
(ii)	(i)	(iii)	10.55	0.00	101.52
(iii)	(ii)	(iii)	5.58	0.00	53.65

3 3D pose estimation based on the ellipsoid-approximated bone model

This chapter presents the three dimensional bone pose reconstruction procedure based on three rigidly attached ellipsoids. First, the constraint equations of the planar system described in the previous chapter are extended to 3D, which can be numerically solved by a subsequently introduced optimization cost function. The chapter finishes with a sensitivity analysis of the cost function, examining the influence of perturbed input variables on the resulting bone pose.

3.1 Formulation of the constraint equations

The 3D rigid body bone model consists of three ellipsoids that are each palpated by a planar pressure sensor. In the following, due to their similarities, the constraint equations will be derived for a general pair $i = 1, \ldots, 3$ of ellipsoid and pressure sensor plane, as shown in Fig. 3.1.

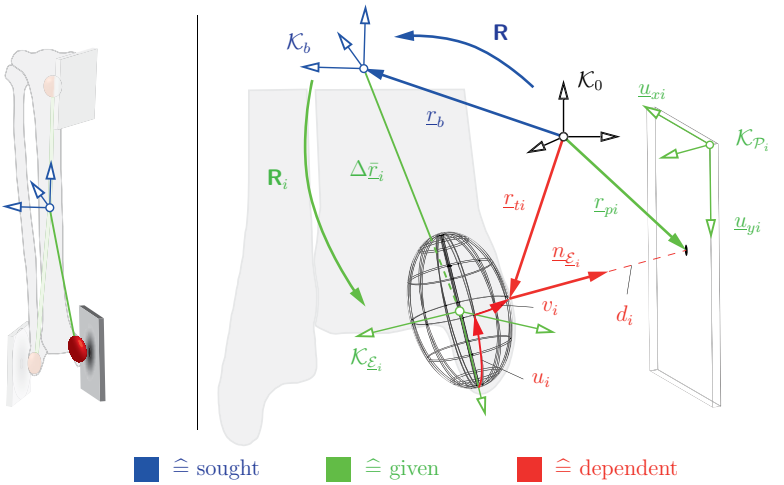

Figure 3.1: Description of the ellipsoid-approximated bone model for the example of one pair of ellipsoid and pressure sensor plane at the medial malleolus.

Assume that the rigid body is palpable as an array of three rigid ellipsoids $\underline{\mathcal{E}}_i$, $i = 1, \ldots, 3$, which are rigidly attached to a body-fixed frame $\mathcal{K}_b$. The rigid body pose is described by the rotation matrix $\mathbf{R}$ transforming body-fixed coordinates to coordinates in the inertial frame $\mathcal{K}_0$, and the position $\underline{r}_b = [x_b, y_b, z_b]^{\mathrm{T}}$ from the origin of $\mathcal{K}_0$ to the origin of $\mathcal{K}_b$ in coordinates of $\mathcal{K}_0$. Each ellipsoid has a local coordinate frame $\mathcal{K}_{\underline{\mathcal{E}}_i}$ rigidly attached to it, whose position relative to the body-fixed frame $\mathcal{K}_b$ is given akin to the previous description by the vector $\Delta\underline{\bar{r}}_i$ and the rotation matrix $\mathbf{R}_i$. The surface of each ellipsoid $\underline{\mathcal{E}}_i$ with semi principal axes $\{a_i\,, b_i\,, c_i\}$ can be parametrized with respect to its local frame $\mathcal{K}_{\underline{\mathcal{E}}_i}$ as

$$\underline{\mathcal{E}}_i(u_i, v_i) = \begin{bmatrix} a_i\,\cos(u_i)\cos(v_i) \\ b_i\,\cos(u_i)\sin(v_i) \\ c_i\,\sin(u_i) \end{bmatrix}, \tag{3.1}$$

where u_i and v_i are the spherical coordinates of the ellipsoid with $-\pi/2 \leq u_i \leq \pi/2$ and $-\pi \leq v_i \leq \pi$.

Likewise, let the pose of each pressure sensor plane $\mathcal{P}_i$ be defined by a plane-fixed frame $\mathcal{K}_{\mathcal{P}_i}$ with in-plane orthonormal vectors $\underline{u}_{xi}$ and $\underline{u}_{yi}$. For an arbitrary point $\underline{r}_{ti}$ on the surface of $\underline{\mathcal{E}}_i$ it holds

$$\underline{r}_{ti} = \underline{r}_b + \mathbf{R}\,\Delta\underline{\bar{r}}_i + \mathbf{R}\mathbf{R}_i\,\underline{\mathcal{E}}_i(u_i, v_i)\,. \tag{3.2}$$

Let $\underline{r}_{ti}$ be the extremal ellipsoid point, i. e. with minimal or maximal distance to the pressure sensor plane. Then this point must fulfill two sets of constraints:

1) [Gradient orthogonality] For the gradient of $\underline{\mathcal{E}}_i$ at point $\underline{r}_{ti}$,

$$\underline{n}_{\underline{\mathcal{E}}_i} = \mathbf{R}\mathbf{R}_i \left(\frac{\partial \underline{\mathcal{E}}_i(u_i, v_i)}{\partial u_i} \times \frac{\partial \underline{\mathcal{E}}_i(u_i, v_i)}{\partial v_i} \right) \tag{3.3}$$

it must hold

$$G_{i,x}: \qquad \underline{n}_{\underline{\mathcal{E}}_i}^{\mathrm{T}}\,\underline{u}_{xi} = 0 \tag{3.4}$$

$$G_{i,y}: \qquad \underline{n}_{\underline{\mathcal{E}}_i}^{\mathrm{T}}\,\underline{u}_{yi} = 0\,. \tag{3.5}$$

2) [Distance orthogonality] Also, the distance vector from the measured pressure point $\underline{r}_{pi}$ on plane $\mathcal{P}_i$ to point $\underline{r}_{ti}$ must be normal to the plane $\mathcal{P}_i$:

$$D_{i,x}: \qquad (\underline{r}_{ti} - \underline{r}_{pi})^{\mathrm{T}}\,\underline{u}_{xi} = 0 \tag{3.6}$$

$$D_{i,y}: \qquad (\underline{r}_{ti} - \underline{r}_{pi})^{\mathrm{T}}\,\underline{u}_{yi} = 0\,. \tag{3.7}$$

Collecting all equations for the three ellipsoids gives a system of 12 scalar constraint equations for the 12 unknowns

$$\underline{q} = [\ \underline{r}_b\ \ \underline{\Phi}_b\ \ u_1\ \ v_1\ \ u_2\ \ v_2\ \ u_3\ \ v_3\ ]^{\mathrm{T}}\,, \tag{3.8}$$

where $\underline{\Phi}_b \in \mathbb{R}^3$ are the rotational degrees of freedom defining the orientation of the rigid body frame $\mathcal{K}_b$, taken as roll-pitch-yaw angles (for rotation sequence x-y-z) in the present case.

3.2 Optimization problem

As mentioned in Chapter **2**, the general system of Eqs. (3.4) to (3.7) will yield a plurality of solutions, so that a direct numerical root-solving of these equations would not be feasible due to the poor conditioning and the closeness of solutions with respect to each other. Thus, instead, the problem is solved as an unconstrained optimization problem with a cost function composed of the weighted sum of the squared constraint values and the squared distances $d_i^2 = \| \underline{r}_{ti} - \underline{r}_{pi} \|^2$

$$F(\underline{q}) = \frac{1}{2}\left(\psi_1 \sum_{i=1}^{3} \left\{ G_{i,x}^2 + G_{i,y}^2 \right\} + \psi_2 \sum_{i=1}^{3} \left\{ D_{i,x}^2 + D_{i,y}^2 \right\} + \psi_3 \sum_{i=1}^{3} {d_i}^2 \right)\,, \tag{3.9}$$

where the weights ψ_i are defined such as to balance between preciseness (first two terms) and feasibility (d_i), and also to homogenize units among terms.

3.3 Sensitivity analysis

For sensitivity analysis, a simulation of bone pose estimation using the optimization cost function from Eq. (3.9) was carried out with a noisy input signal. It covers small variations of all input variables comprising position and orientation (for rotation sequence x-y-z) of the sensor frames $\mathcal{K}_{\mathcal{P}_i}$, relative pressure point coordinates $\underline{r}_{pi}$, ellipsoid centers $\Delta\underline{\bar{r}}_i$ and ellipsoid semi principal axes $\{a_i\,, b_i\,, c_i\}$ (see Fig. 3.2). The noise-free input variables originate from the flexion/extension measurement presented in Chapter **5** and are summarized in Table B.1.1 to Table B.1.2 in the Appendix. Starting from a given reference pose (see Table B.1.3 in the Appendix), input variables were overlaid with Gaussian white noise with a mean value $\mu = 0.0$ and a standard deviation $\sigma = 0.15$, producing an error Δe of approximately 1 mm in position and 1° in orientation. For each of these variations, the new pose was computed by re-applying the optimization run with: (1) weights $\psi_1 = \psi_2 = \psi_3 = 1.0$ and (2) weights

$\psi_1 = \psi_2 = 1.0, \psi_3 = 0.0$ i. e. by switching on and off the feasibility term d_i respectively. Optimization was performed using the routine `e04unc` of the *Numerical Algorithms Group C library* [71] where all options (i. e. tolerances, step limits, etc.) were left in its default settings.

The deviations of the solutions were regarded as first-order variations $\Delta\underline{r}_e$ for translation and $\Delta\underline{\Phi}_e$ for rotations. Both were then coupled using the concept of the characteristic length κ [57] (firstly introduced in Section **2.4.4**), yielding the equivalent translational change

$$\Delta s = \|\Delta\underline{r}_e\| + \kappa \cdot \|\Delta\underline{\Phi}_e\| \quad \text{with} \quad \kappa = \sqrt{2\ell_{\max}^2(1-\cos(\pi/180))}\,, \tag{3.10}$$

where $\ell_{\max} = 186.78$ mm is the distance between the rigid body center $\mathcal{K}_b$ to the furthest ellipsoid center, giving in the present case $\kappa = 3.26$ mm. The resulting errors for 10^5 data points are shown in Fig. 3.3. It can be seen that for all cases the order of the output error remains in the same order of magnitude as the input noise. Without feasibility term, input errors are amplified by a factor of 1.25 for sensor poses (note that sensor poses comprise both, position and orientation errors at the same time), 2.5 for relative pressure point coordinates, 2 for ellipsoid centers and 1.5 for the semi axes. In contrast, using the optimization cost function including the feasibility term d_i, amplification factors are significantly reduced to 1.0 for sensor poses, 0.6 for relative pressure point coordinates, 0.8 for ellipsoid centers and 0.6 for the semi axes.

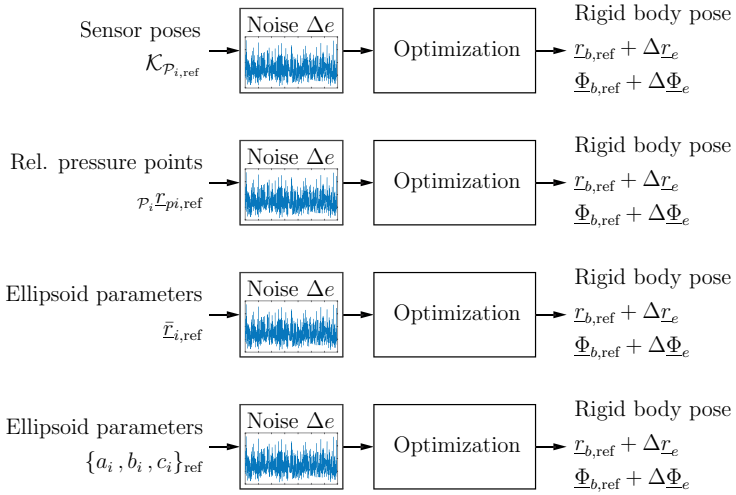

Figure 3.2: Sensitivity analysis of the optimization process, $i = 1, \ldots, 3$.

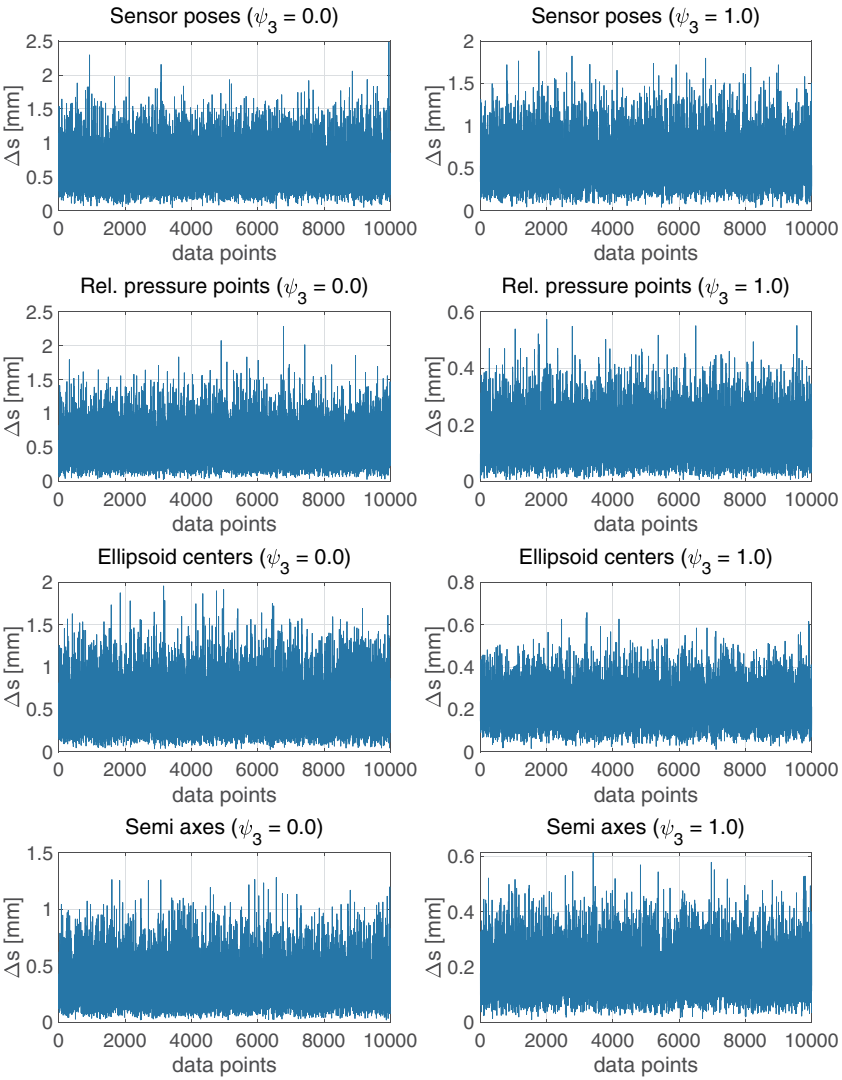

Figure 3.3: Sensitivity analysis of the optimization cost function without (left) and with (right) feasibility term d_i varying (from top to bottom): sensor poses, rel. pressure point coordinates, ellipsoid centers and semi principal axes.

4 Self-adjusting point for bone pose estimation

In this chapter, a special case of the 3D bone pose estimation procedure presented in Chapter **3** is analyzed, namely the limiting case where all ellipsoid semi principal axes tend to zero such that ellipsoids become points. First, the 3D model will be described, followed by the introduction of an automatable procedure which allows the approximation of the rigid body geometry based on data from a previously performed bone pose measurement. At the end of this chapter, the approximation-error expectation of this case will be discussed.

4.1 Three-point model description

The three-point-approximated bone model as a simplified version of Fig. 3.1 (see Section **3.1**) by transforming all ellipsoids into points is shown in Fig. 4.1. This problem is similar to the 6 degrees of freedom parallel manipulator whose direct and inverse kinematics analysis was determined by Chen et al. [17], the latter yielding 8 different real solutions in general.

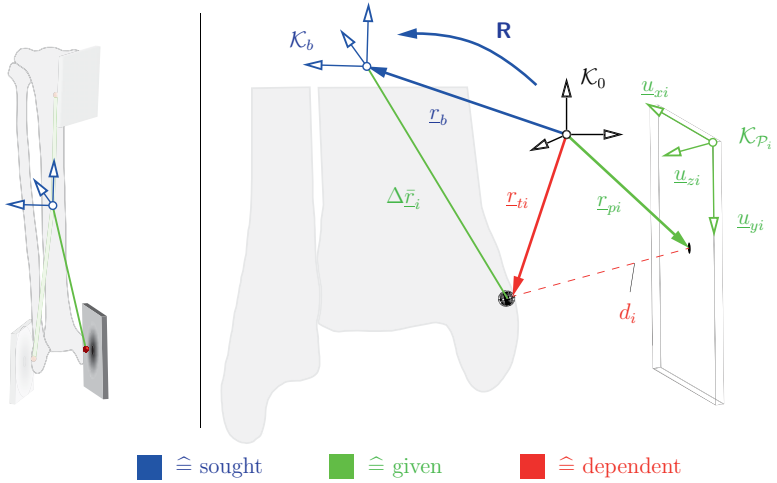

Figure 4.1: Description of the three-point-approximated bone model for the example of one pair of point and pressure sensor plane at the medial malleolus.

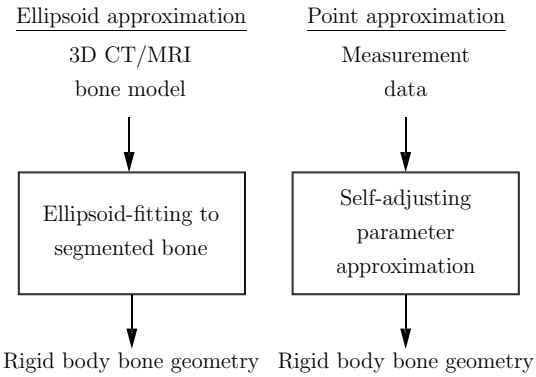

Figure 4.2: Comparison of the rigid body bone geometry determination between ellipsoid- and point-approximated bone model.

4.2 Self-adjusting parameter approximation

In a real application, the ellipsoid-approximated bone geometry can be determined e. g. from a 3D CT/MRI scan. This section presents an alternative method that allows to approximate the rigid body geometry of a point-approximated bone model by means of a previously performed bone pose measurement (see Fig. 4.2). In this way, additional radiation exposure to the subject concerned can be avoided and, moreover, the parameter assessment of the rigid body is fully automated.

Let $n = 1, \ldots, N$ be a given set of pressure sensor plane configurations comprising sensor poses $\mathcal{K}^n_{\mathcal{P}_i}$ and relative pressure point coordinates $\underline{r}^n_{pi}$, with $i = 1, \ldots, 3$. Then, as shown in Fig. 4.3 and Fig. 4.4, by assuming that the distance d^n_i is known, forward kinematics can be used in order to compute the rigid body point coordinate $\underline{r}^n_{ti}$ from

$$\underline{r}^n_{ti} = \underline{r}^n_{pi} + \underline{u}^n_{zi} \cdot d^n_i \,. \tag{4.1}$$

Let $\mathcal{K}^n_b$ be the frame attached to the rigid body, its position $\underline{r}^n_b$ and orientation $\mathbf{R}^n$ can be defined as follows:

(i) The origin $\underline{r}^n_b$ is defined as the centroid of the three point coordinates $\underline{r}^n_{t1}$, $\underline{r}^n_{t2}$ and $\underline{r}^n_{t3}$.

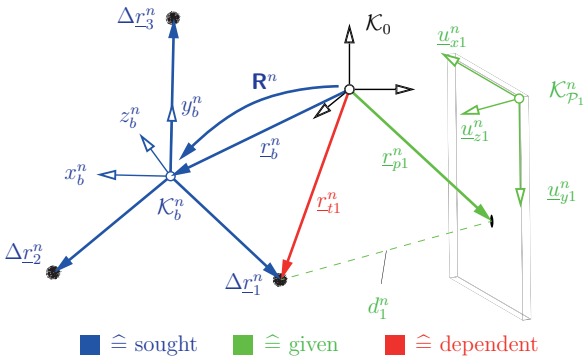

Figure 4.3: Construction of $\mathcal{K}_b^n$ using forward kinematics.

(ii) The y-axis points toward point $\underline{r}_{t1}^n$.

(iii) The x-axis lies inside the plane defined by the three point coordinates $\underline{r}_{t1}^n$, $\underline{r}_{t2}^n$ and $\underline{r}_{t3}^n$ and points toward $\underline{r}_{t2}^n$.

(iii) The z-axis is defined according to the right-hand rule.

From that, the relative position $\Delta\underline{r}_i^n$ of each point with respect to the body-fixed frame $\mathcal{K}_b^n$ can be computed from

$$\Delta\underline{r}_i^n = (\mathbf{R}^n)^{\mathrm{T}}(\underline{r}_{ti}^n - \underline{r}_b^n)\,. \tag{4.2}$$

Finally, the global rigid body parameter $\Delta\bar{\underline{r}}_i$ can be approximated by averaging the relative position vector $\Delta\underline{r}_i^n$ over all measured data points $n = 1, \ldots, N$

$$\Delta\bar{\underline{r}}_i = \frac{1}{N}\sum_{n=1}^{N}\Delta\underline{r}_i^n\,. \tag{4.3}$$

4.3 Approximation-error expectation

The self-adjusting point method assumes that the protuberance point effecting the pressure point is more or less always the same. This is the case if the transverse relative rotations of the pressure plane about its in-plane orthonormal vectors $\underline{u}_x$ and $\underline{u}_y$ with respect to the bone are zero or very small. If this is not the case, a relative rolling of the pressure plane occurs with respect to the contact face of the protuberance, which leads to a variation of the contact point with respect to the bone (see Fig. 4.5).

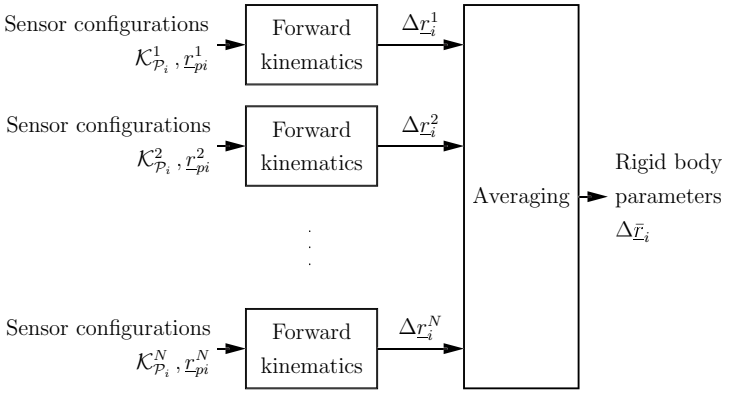

Figure 4.4: Rigid body parameter approximation based on N measured pressure sensor plane configurations, $i = 1, \ldots, 3$.

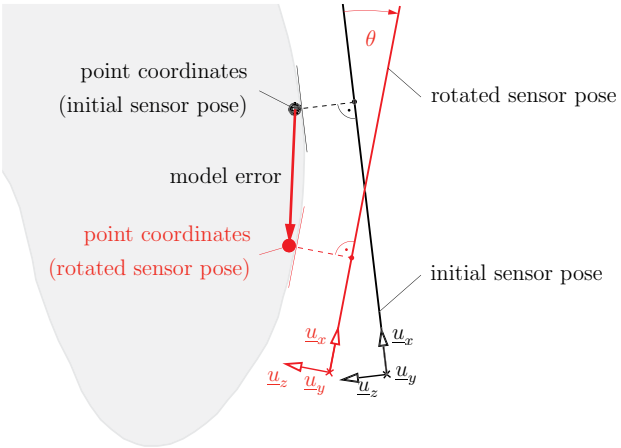

Figure 4.5: Point-approximated bone model error for relative rotations of the sensors about its in-plane orthonormal vectors.

In the following, when using the point-approximated bone model, it is assumed that transverse rotations of the pressure planes with respect to the bone are very small and thus the constant pressure point assumption is true. The validation of this assumption is discussed in Section **5.4**.

5 Validations

This chapter describes the validation of the previously introduced method for bone pose determination by palpating three prominent bone protuberances through tracked pressure sensors. The first section presents the validation of the pressure mapping system used to determine the pressure point from a given pressure distribution. Then, the ellipsoid-approximated bone model is validated using dual fluoroscopy. This section specifies in detail the methodology used to manually register fluoroscopy images along with the results of three basic movements of the shank: flexion/extension, abduction/adduction and internal rotation. Finally, the differences in bone poses between point- and ellipsoid-approximated bone model are further investigated in the last section.

5.1 Pressure mapping

The identification of the pressure point consists of three basic blocks (Fig. 5.1). First, the pressure sensor pose is determined using a marker tracking system, so that each sensel on the sensor can be converted into absolute coordinates and the normal vector to the sensor plane is known. Then, by pressing the sensor on the bone protuberance, the relative position of the pressure point on the sensor is determined from the given pressure distribution. This procedure was validated experimentally with a *Kuka KR6/2* robot.

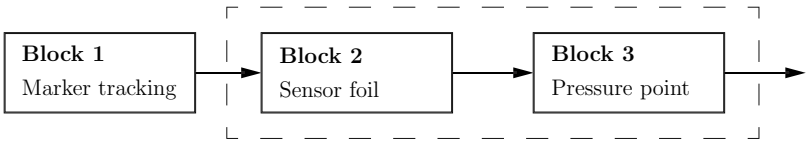

Figure 5.1: Basic blocks for pressure point identification.

5.1.1 Materials and Methods

For marker tracking (block 1), three cameras of the *A.R.T.* camera system (*ARTTRACK1*) were used [1].

For the pressure foil (block 2), a 27.9 mm × 27.9 mm *Tekscan* pressure mapping sensor

5027 with $44 \times 44 = 1936$ sensels was used. The sensels are arranged in a 44×44 equally spaced grid with a sensel spacing of ± 0.6 mm [70]. Each sensel reports a binary pressure value p^B from 0 to 255 which is linearly scaled to a physical pressure range, in our case 0–34.5 N/cm^2. The pressure values are stored in a 44×44 matrix, where each element represents a sensel of the grid.

The relative pressure point (block 3) is computed at each time step by five basic operations done using computer vision software *OpenCV*, [11]). This is exemplarily shown in Fig. 5.2 for a typical pressure distribution of a pressure foil attached to the lateral malleolus of a test person:

(O1) Smoothing the data using the bilateral filter `cv::bilateralFilter` with a filter size of $d = 9$ pixels and sigma values both set to $\sigma_{\text{color}} = \sigma_{\text{space}} = 111$.

(O2) Determining the maximum binary pressure value $p^B_{\max}$ over all sensels (function `cv::minMaxLoc`).

(O3) Zeroing all sensels with pressure below $(p^B_{\max} - \Delta p^B)$, Δp^B adjusting the edge thickness of the highest pressure plateau, in the present case chosen as 80.

(O4) Determining the largest contour of all remaining areas (using `cv::findContours`).

(O5) Computing the center of pressure of the largest contour inner area.

The purpose of the operations (O1) to (O4) is to exclude pressure values from the pressure distribution caused by skin contact in the neighborhood of the bone protuberance. Once excluded, the center of pressure of the remaining pressure distribution is assumed to be the closest point on the sensor foil to the bone surface under the skin, which is determined in operation (O5).

The resolution error of block 3 can only be determined together with block 2. To this end, a pressure sensor foil was placed on a flat surface whose sensor grid frame $\mathcal{K}_G$ was tracked by the *A.R.T.* camera system with respect to the inertial frame $\mathcal{K}_0$ (Fig. 5.3). A thin foam layer was placed on top of the pressure foil in order to obtain a larger contact area, emulating skin-on-bone effects. For a given pressure distribution, the relative pressure point ${}_G\underline{r}_p$ can be computed by the previously described 5 operations. Thus, the pressure point can be calculated as

$$\underline{r}_p = \underline{r}_G + {}_G\underline{r}_p \,. \tag{5.1}$$

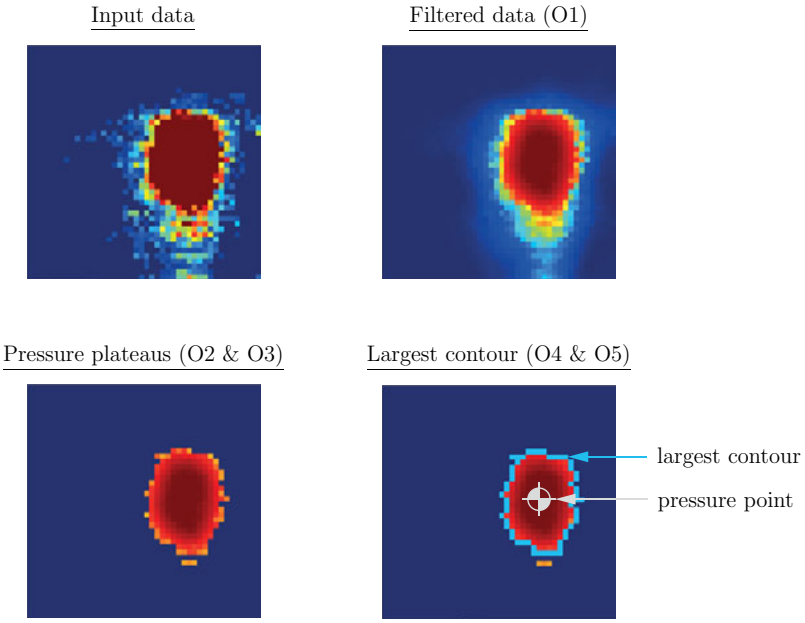

Figure 5.2: Example of a pressure point computation from a given pressure distribution.

Furthermore, a metal sphere was dragged along the foam using a *Kuka KR6/2* robot, in such a way that the orientation of the sphere fixed frame $\mathcal{K}_S$ remained constant during measurement within the robot accuracy tolerances (Fig. 5.3, (Front view)). The pose $\mathcal{K}_S$ of the sphere was tracked with the *A.R.T.* camera system. The constant position vector ${}_S\underline{r}_c$ from $\mathcal{K}_S$ to the closest point c on the sphere with respect to the sensor foil was determined by an initial calibration. Therefore, the sphere was positioned directly on the pressure sensor (with foam removed) such that both points c and the lower left sensel at the origin of frame $\mathcal{K}_G$ of the pressure sensor coincide (see Fig. 5.4). In this case, only the lower left sensel is measuring pressure, so that ${}_G\underline{r}_p = 0$. Finally, the vector $\underline{r}_c$ was calculated serving as a reference, where

$$\underline{r}_c = \underline{r}_S + {}_S\underline{r}_c\,. \tag{5.2}$$

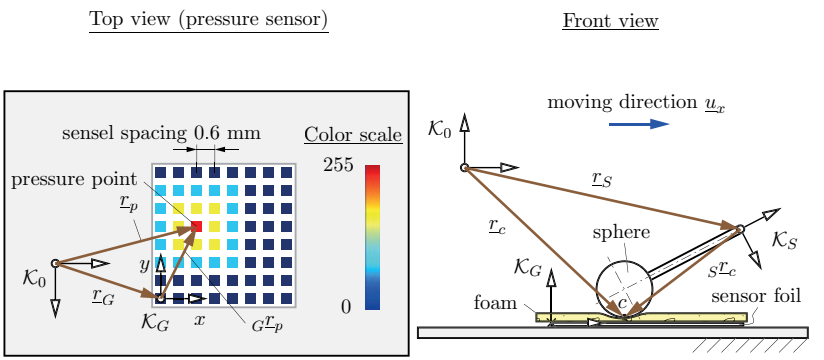

Figure 5.3: Schematic representation of the experimental setup of the pressure sensor (left) and the reference sphere dragged by the *Kuka* robot (right).

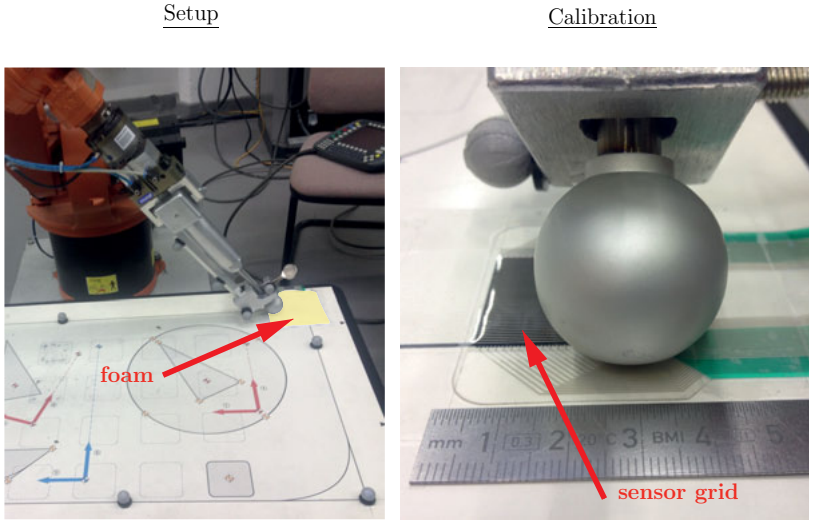

Figure 5.4: Picture of the experimental setup (left) and the calibration process (right).

5.1.2 Results

The upper plots of Fig. 5.5 show the resulting x- and y-positions of the *Kuka* reference (red line) and the calculated pressure point (blue line). It can be seen that the pressure point curve is much spikier compared to the reference, with maximum amplitudes of approximately 0.3 mm. For both directions the total deviation stays below 0.3 mm during the whole measurement (lower plots of Fig. 5.5) with a root mean square error of 0.10 mm in x- and 0.09 mm in y-direction. For the identifica-

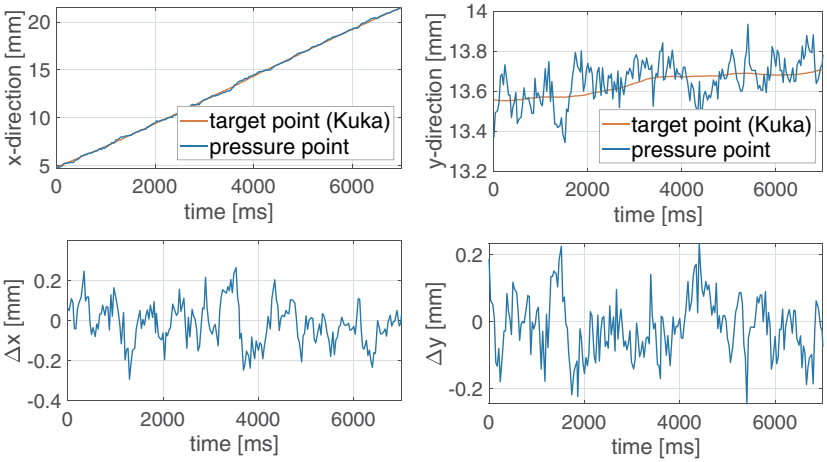

Figure 5.5: Comparison between target and computed pressure point position (top) and quantification of their translational deviations (bottom) in x-direction (left) and y-direction (right).

tion of the pressure point, multiple filters have been validated in the bachelor thesis of Yang [72], namely `cv::AdaptiveThreshold`, `cv::bilateralFilter`, `cv::boxFilter`, `cv::dilate`, `cv::erode`, `cv::GaussianBlur`, `cv::medianBlur` and `cv::morphologyEx`. By comparing root mean square deviations, it could be shown that the bilateral filter was the most accurate filter among all others.

5.1.3 Discussion

The results suggest that pressure points can be identified with a precision of approximately 0.3 mm, which is half of the sensel spacing of 0.6 mm of the *Tekscan* sensor.

It can be assumed that the sensel spacing has the biggest impact on the resulting precision, however - to the authors knowledge - currently no pressure sensor foil with a smaller sensel spacing exists. The discontinuous sensels also result in spiky pressure point positions, which can be smoothed in later applications in order to pass smoother input data on to the optimizer.

The bilateral filter whose characteristic is to preserve edges during the filtering process turned out to be the most accurate one to determine the pressure point from a given pressure distribution. The preservation of edges is particularly important for pressure distributions affected by noisy data in the neighborhood of the pressure point caused by skin contact, as is the case here.

This validation uses a motion capture system in order to compute the reference position of the pressure point. The accuracy of marker tracking systems depends on many parameters such as camera setup, camera resolution, movement condition (static and dynamic), room temperature, etc. However, it was experienced that instrumental errors cannot generally be quantified based on the knowledge of those system parameters, as it is also dependent on the specific task that is captured (see Section **1.2**). Thus, it is not possible to state the exact accuracy of the marker system during this experiment. Here, it was assumed that the marker tracking error is negligible with respect to the pressure point computation error.

5.2 Ellipsoid-approximated bone model validation

This section presents the validation of the bone pose estimation algorithm based on the ellipsoid-approximated bone model using dual fluoroscopy. The concept of this validation is, first, to determine simultaneously the bone fixed coordinate frames $\mathcal{K}_{b,\mathrm{PS}}$ and $\mathcal{K}_{b,\mathrm{DF}}$ of a real shank motion using the pressure sensor system (PS) and the dual fluoroscopy system (DF) respectively. And second, to determine the translational $\Delta\underline{r}_b$ and rotational deviations $\Delta\underline{\Phi}_b$ between both frames (see Fig. 5.6).

5.2.1 Materials and Methods

One participant (sex: male, age: 34, height: 173 cm, weight: 82 kg, no injuries) volunteered to perform three different movement patterns of the right shank: (1) flexion/extension, (2) abduction/adduction and (3) internal rotation of the knee, each of

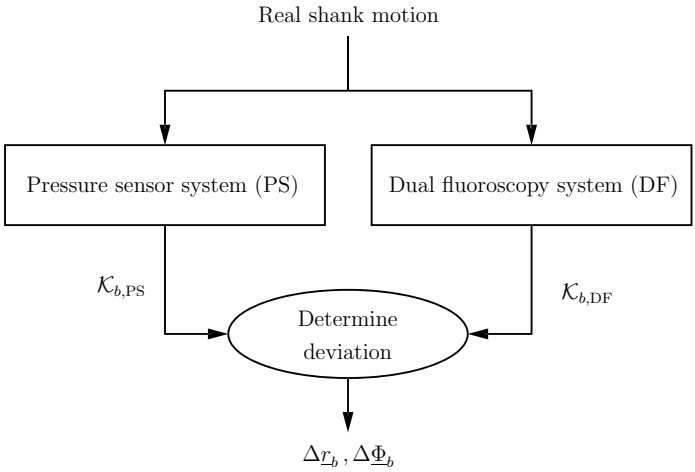

Figure 5.6: Concept of the ellipsoid-approximated bone model validation using dual fluoroscopy.

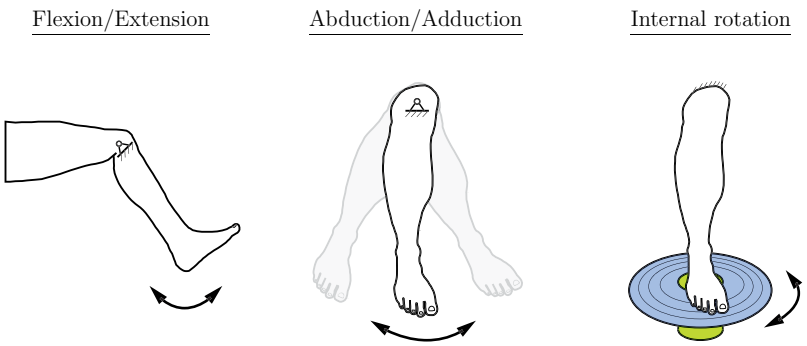

Figure 5.7: Idealized shank movement patterns performed during data acquisition.

which was repeated approximately three times back and forth (limited by the allowed radiation duration). Fig. 5.7 schematically shows the idealized movement patterns. The Conjoint Health Research Ethics Board approved this study, and written informed consent was obtained from the participant before the experiment.

Pressure Sensor System

The general setup of the pressure sensor system is schematically shown in Fig. 5.8. Three *Tekscan* 5027 pressure sensor foils [70] were used for palpating bone protuberances. Each sensor was attached to a support plate made of hard plastic which was placed on the right shank of the participant using adhesive tape. The predefined locations were (1) the tibial tuberosity, (2) the lateral malleolus and (3) the medial malleolus (see Fig. 5.9). Elastic straps were tied around each support plate in order to produce pressure distributions that could be quantified. Pressure data was captured at approximately 20 Hz. The identification of the pressure point from a given pressure distribution was carried out as described in Section **5.1**.

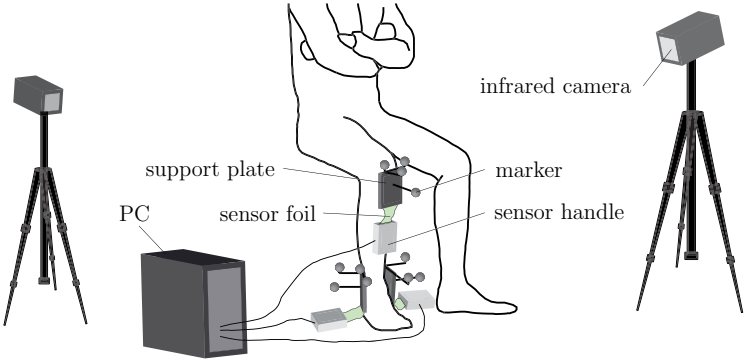

Figure 5.8: Schematic representation of the experimental setup of the pressure sensor system.

Rigid body bone model

A 3D bone model was generated from a computed tomography scan of the examined bone using the software *Amira* [65]. Ellipsoids were visually fitted to the bone protuberances of the 3D bone model with the *Mobile-C++ library* [38], as shown exemplarily in Fig. 5.10 for the tibial tuberosity. The rigid body parameters obtained are summarized in the Appendix in Table C.4.1 for flexion/extension and abduction/adduction, and in Table C.4.2 for internal rotation with respect to the bone fixed coordinate frame $\mathcal{K}_b$. The frame $\mathcal{K}_b$ is hereby defined such that the origin lies approximately in the center of all three ellipsoid centers, the local y-axis points along the tibial shaft in the prox-

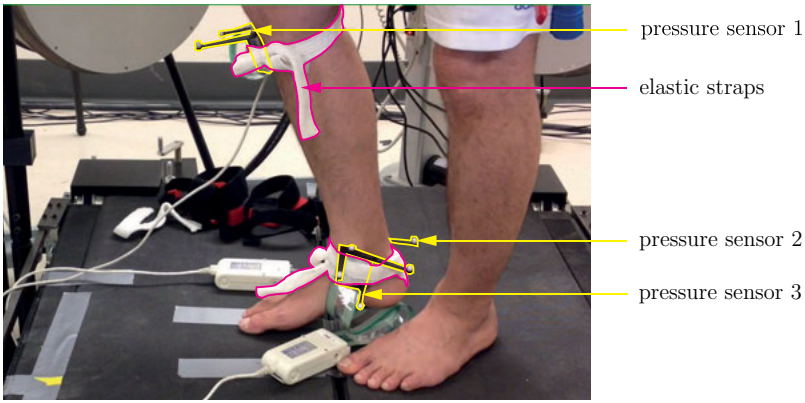

Figure 5.9: Picture of the sensor placement on the right shank.

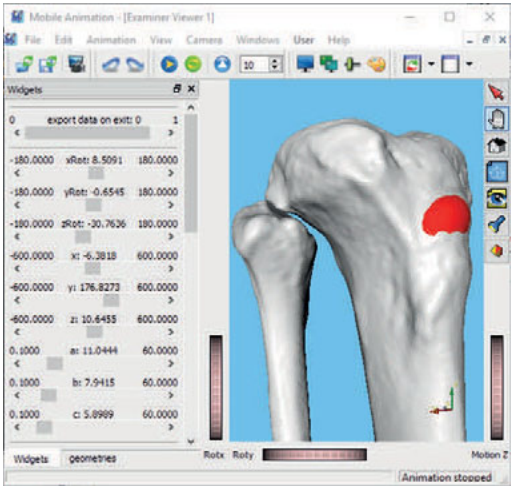

Figure 5.10: Screenshot of an ellipsoid fitting at the tibial tuberosity with *Mobile-C++* [38].

imal, the x-axis in the lateral, and the z-axis in the posterior direction, respectively. The parameters for internal rotation differ from the other movement patterns, as the pressure sensors had to be slightly shifted for this case to avoid artifacts caused by tendons between sensor and bone.

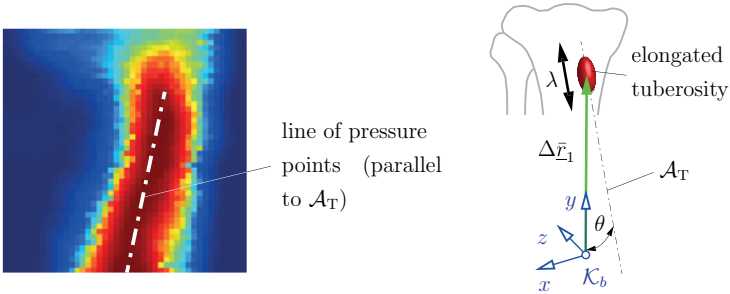

Figure 5.11: Typical filtered pressure distribution at the tibial tuberosity (left) and description of the longitudinal axis of tuberosity (right).

The participant's bone protuberance at the tibial tuberosity had a narrow but longitudinal shape resulting in pressure distributions as depicted for a typical example in Fig. 5.11. As a consequence, the contact relevant region of the bone surface was represented by a line instead of a point. For this reason, an additional degree of freedom λ was introduced allowing the ellipsoid center $\Delta\underline{\bar{r}}_1$ (located at the tibial tuberosity) to move freely along the longitudinal axis of tuberosity $\mathcal{A}_\mathrm{T}$ as shown in Fig. 5.11. For all three motions, the axis $\mathcal{A}_\mathrm{T}$ was defined such that (1) it intersects with the ellipsoid center $\Delta\underline{\bar{r}}_1$, (2) it lies in the yz-plane of the bone fixed frame $\mathcal{K}_b$ and (3) is rotated positively around the x-axis by the angle $\theta = 5.4°$. The vector $\underline{q}$ of Eq. (3.8) was thus extended to

$$\underline{q} = [\, \underline{r}_b \;\; \underline{\Phi}_b \;\; u_1 \;\; v_1 \;\; u_2 \;\; v_2 \;\; u_3 \;\; v_3 \;\; \lambda \,]^\mathrm{T} . \tag{5.3}$$

Optimization was performed using the routine `e04unc` of the *Numerical Algorithms Group C library* [71] where all options (i. e. tolerances, step limits, etc.) were left in its default settings. Weighting factors of the cost function Eq. (3.9) where chosen as $\psi_1 = \psi_2 = \psi_3 = 1.0$.

Dual fluoroscopy imaging system

The dual fluoroscopy system described by Lichti et al. and Sharma et al. [43, 62] was used to collect proximal tibia and fibula motion in *Normal Mode* at 30 Hz (see Fig. 5.12 for a picture of the laboratory). To reduce radiation exposure, the recording period was 3 seconds, during which the participant made approximately two to three repetitions of each movement pattern. In advance, the maximal dose rate of one data collection was

estimated with a dose meter to 0.02 mSv. Fig. 5.13 schematically shows the setup of the dual fluoroscopy system: both image intensifiers were placed parallel to the ground with an interbeam angle of 60° and a distance of approximately 56 cm and 61 cm away from the shank at the point of intersection of both beams. Bone poses identified with the dual fluoroscopy system are described in coordinates of frame $\mathcal{K}_{\mathrm{DF}}$, whose x-axis points from X-ray sources to high speed cameras, z-axis is oriented vertically pointing upward and y-axis is defined according to the right-hand rule (see Fig. 5.13).

The calibration process of the dual fluoroscopy system as well as the postprocessing steps necessary to obtain bone poses from measurement data are described in detail by Sharma et al. [43] and will only be summarized briefly here. Calibration of the dual

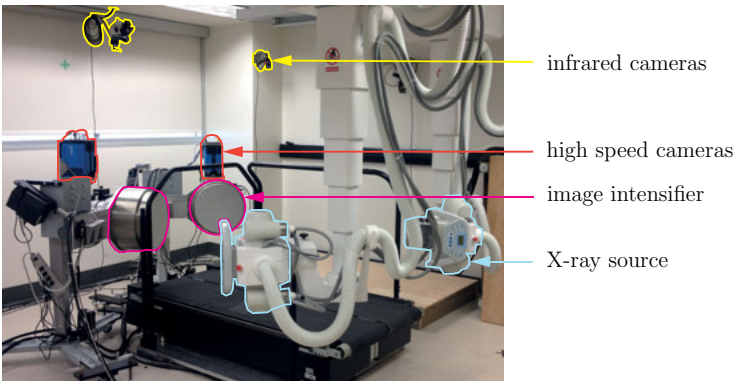

Figure 5.12: Picture of the dual fluoroscopy laboratory setup.

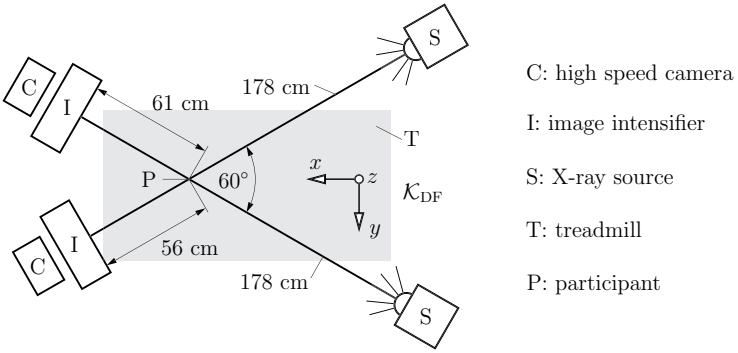

Figure 5.13: Schematic representation of the dual fluoroscopy experimental setup.

fluoroscopy system was done with bead picking root mean square error of 0.008 mm ± 0.002 mm using a custom acrylic cube with bead locations. Distortion correction for all images was completed using the program *Undistortion* (Brown University, Rhode Island, USA) [12]. For dual fluoroscopy image contrast and bone edge enhancement the adaptive histogram equalization algorithm `adapthisteq` from *MATLAB* was used [48].

Bone poses were determined with model based manual 2D-3D registration technique using the 3D CT bone model [7, 8, 9, 32, 40, 41, 75]. For all movement patterns, 2D-3D registration was performed on a *LG24EA53* 24 inch full HD display on highest brightness and contrast settings using the software *JointTrack Biplane* (University of Florida, Gainesville, Florida, USA). The first image of each motion sequence was registered from its original position, i. e. at the origin of the laboratory coordinate frame $\mathcal{K}_{\mathrm{DF}}$. Then, subsequent images were registered by using the pose of the previous image as a first initial guess.

Marker-based motion capture system

The motion capture system *Motion Analysis* was used to collect marker positions allowing to determine the absolute position and orientation of each pressure sensor foil. Eight cameras (4x Kestrel, high resolution: 2048x1088, 4x Osprey cameras, mid resolution: 640x480) were placed around the participant (see Fig. 5.14).

To calibrate the relative position of a sensor grid with respect to the *Motion Analysis* reference frame, a calibration pencil equipped with markers was used whose dimensions were known with a manufacturing tolerance of 50 μm (see Fig. C.1.1 in the Appendix). Calibration was done by sliding the tip of the pencil over a fixed sensor plane while simultaneously tracking both marker sets: the first attached to the pencil and the second attached to the pressure sensor.

To calibrate the relative transformation ${}^{\mathrm{DF}}\mathbf{T}_{\mathrm{MA}}$ between dual fluoroscopy and *Motion Analysis* system, a calibration frame box equipped with 12 markers was used (see Fig. 5.15). The calibration was performed by taking a dual fluoroscopy image of the frame box while simultaneously measuring the position of all 12 markers with the camera system. After 2D-3D registration of the frame box, the transformation matrix between both systems was determined.

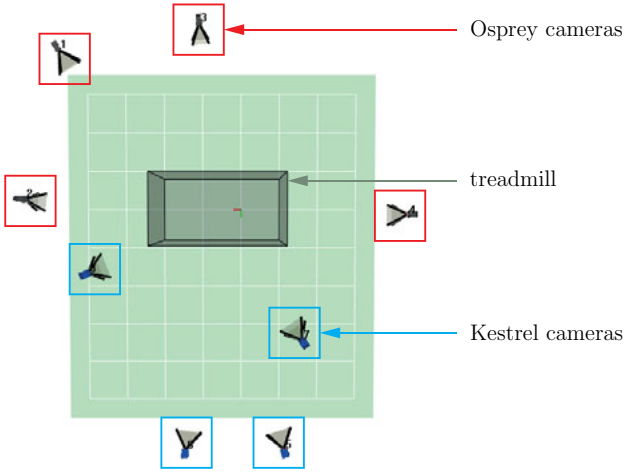

Figure 5.14: Schematic representation of the *Motion Analysis* camera setup.

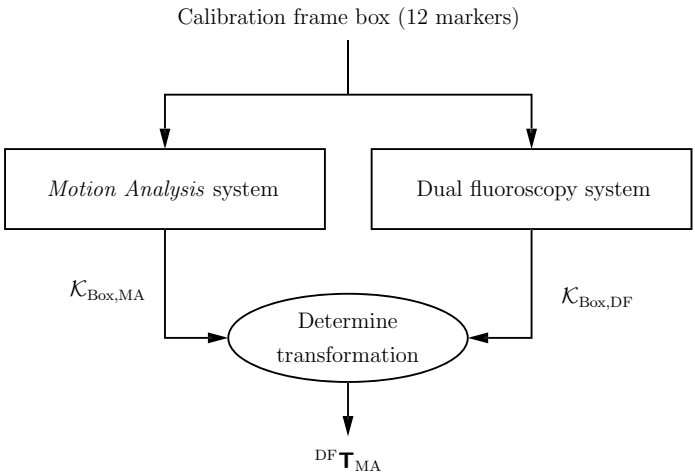

Figure 5.15: Calibration of the dual fluoroscopy (DF) system with respect to the *Motion Analysis* (MA) system.

Data synchronization

Data coming from the dual fluoroscopy system and the *Motion Analysis* system were synchronized with an analog signal triggered manually during data acquisition (see Fig. 5.16). Furthermore, the analog signal as well as the pressure sensor system were synchronized to the PC clock. Data points from all systems were synchronized by linear interpolation.

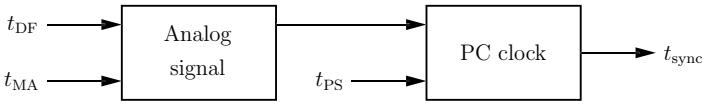

Figure 5.16: Data synchronization between dual fluoroscopy (DF), *Motion Analysis* (MA) and pressure sensor system (PS).

5.2.2 Results without initial guess

The comparison between both systems was evaluated as relative pose deviation from pressure sensor to dual fluoroscopy system in mm for translations and degree for rotations. Rotational deviations were assumed as very small and thus as vectors $\Delta\underline{\Phi}_b = [\Delta\Phi_{b,x}, \Delta\Phi_{b,y}, \Delta\Phi_{b,z}]^{\mathrm{T}}$ according to EULER's Theorem for small rotations. The results shown in Fig. 5.17 are described in coordinates of the dual fluoroscopy coordinate frame $\mathcal{K}_{\mathrm{DF}}$. During the experiments, some time intervals did not yield correct values due to disappearance of medial ankle pressure sensor marker positions from the camera's field of view. Also, during internal rotation, the tibial tuberosity lost contact with the pressure sensing area for a small period of time. These periods are highlighted with gray bars respectively and were excluded from the evaluation.

Maximal deviations between the manually registered dual fluoroscopy and pressure sensor poses were identified at approximately 5 mm and 2° for flexion/extension, 3 mm and 1.4° for abduction/adduction, 6 mm and 3.5° for internal rotation motion. Table 5.1 summarizes the root mean square deviations (RMSD) of all values shown in Fig. 5.17 to compare with other publication presented in Section **1.2**. It can be seen that RMSDs vary from 0.13 mm to 1.63 mm in translation and 0.78° to 2.66° in rotation, the largest deviations occurring during internal rotation. Furthermore, Fig. 5.18 shows the resulting optimal solution of the optimization cost function for all three motions. All residuals are separately illustrated in the Appendix in Fig. C.2.1 to Fig. C.2.3.

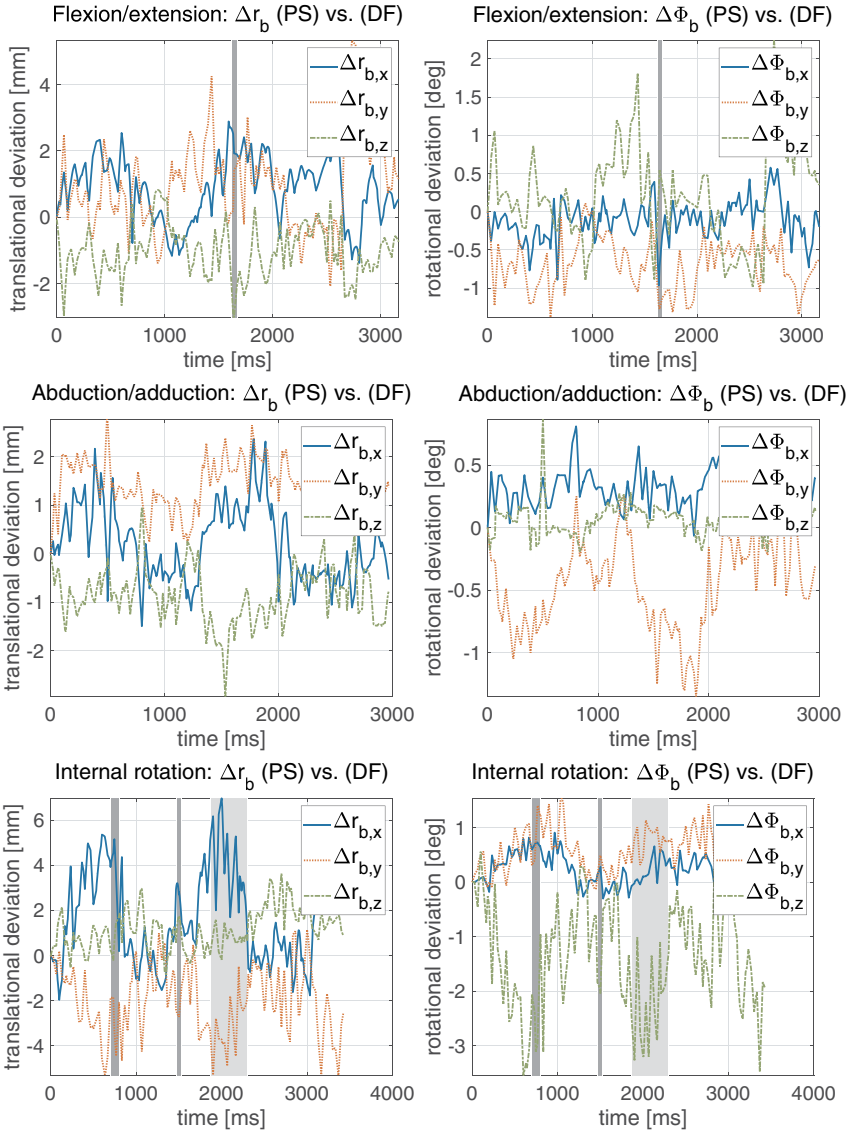

Figure 5.17: Translational (left) and rotational deviations (right) between pressure sensor (PS) and dual fluoroscopy system (DF).

Table 5.1: Root mean square deviations (RMSD) between pressure sensor and dual fluoroscopy system.

Movement pattern	RMSD [mm]			RMSD [deg]		
	$\Delta r_{b,x}$	$\Delta r_{b,y}$	$\Delta r_{b,z}$	$\Delta\Phi_{b,x}$	$\Delta\Phi_{b,y}$	$\Delta\Phi_{b,z}$
Flexion/extension	0.25	0.74	0.69	1.26	1.70	1.23
Abduction/adduction	0.38	0.58	0.13	0.78	1.54	1.02
Internal rotation	0.33	0.67	1.63	2.66	2.48	1.44

One can see that optimal solutions are in the range of 1.5 mm^2 to 3.5 mm^2 for flexion/extension, 4.5 mm^2 to 7 mm^2 for abduction/adduction and 0 mm^2 to 1 mm^2 for internal rotation.

5.2.3 Results with initial guess

As shown in the example of Fig. 5.19-(1) (registered image of one camera at $t = 3270$ ms during internal rotation), visual analysis of the manual registered images showed still large discrepancies between the projected 3D CT bone model (solid blue lines) and the tibia and fibula bone contours (dotted yellow and dash-dotted brown lines respectively) that could not further be improved manually. This was due to the fact that manual registration requires rotations of the CT volume in 3D using Euler angles to match the dual fluoroscopy projections, which is unintuitive to accomplish. For this reason, in the following, the pressure sensor results were used to find better initial guess poses for manual registration (Fig. 5.19-(2a)), so that remaining rotations were very small and thus nearly commutative. In this way, an ensuing manual 2D-3D registration could be performed resulting in visually near-to-perfect fitting contours between projected 3D CT bone model and the underlying fluoroscopy image (see Fig. 5.19-(2b)).

The results for manual 2D-3D registration with initial guess are displayed in Fig. 5.20. One can see that the pressure sensor poses differs from the dual fluoroscopy poses, apart from outliers, in the order of magnitude of 0.6 mm and 0.2° for flexion/extension, 0.5 mm and 0.3° for abduction/adduction, and 1.0 mm and 0.6° for internal rotation. Table 5.2 summarizes the root mean square deviations (RMSD) of all values shown in Fig. 5.20. It can be seen that RMSDs stay below 0.38 mm in translation and 0.65° in rotation for all movement patterns.

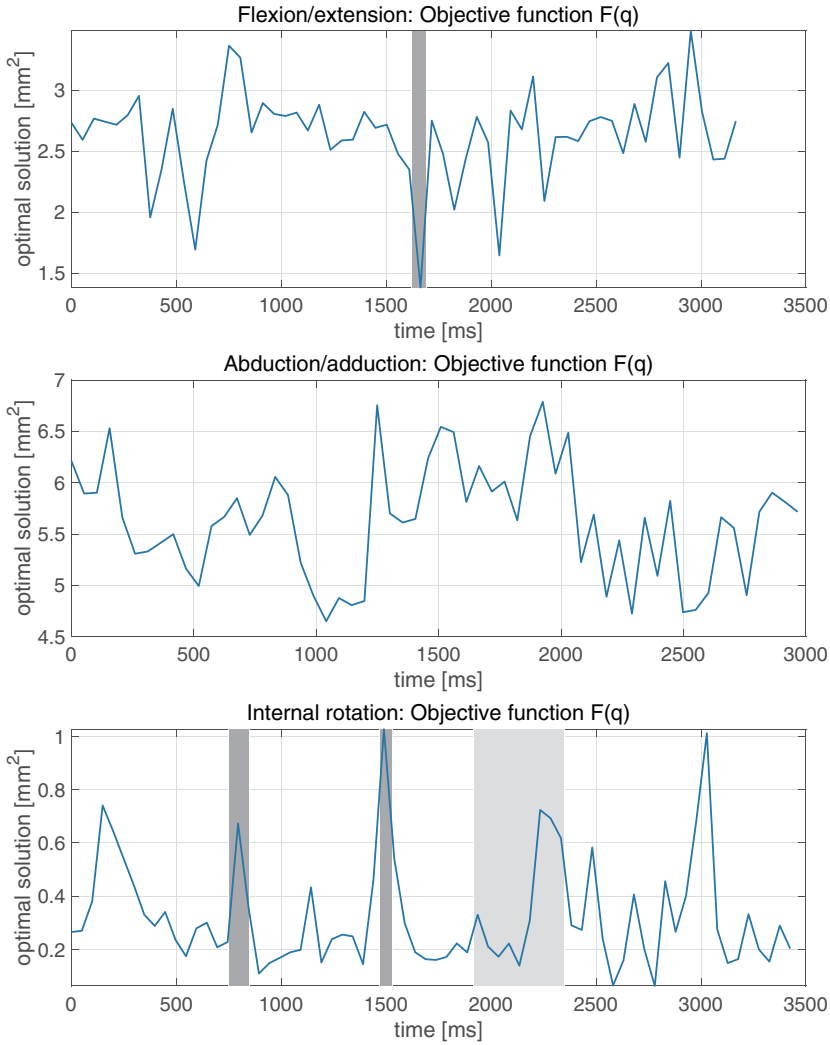

Figure 5.18: Optimal solutions found by the *NAG* optimizer for the ellipsoid-approximated bone model.

5.2.4 Discussion

The validation confirms that shank motion can be quantified by palpating three bone protuberances using pressure sensors with deviations below 1 mm in translation and

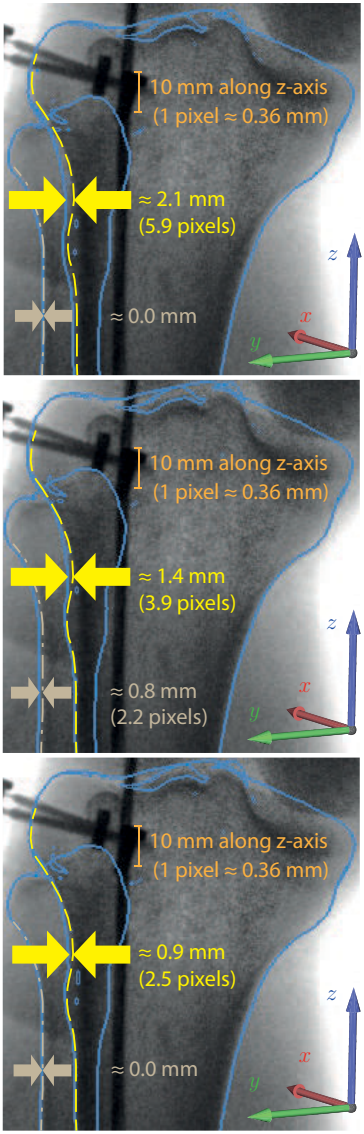

(1) Initial manual registration

(2a) Pressure foil registration

(2b) Pressure foil registration with post manual fine tuning

Figure 5.19: Example 2D-3D registration comparison. Solid blue lines: Projected 3D CT bone model. Dotted and dash-dotted yellow/brown lines: Highlighted tibia and fibula bone contours of the underlying 2D fluoroscopy image.

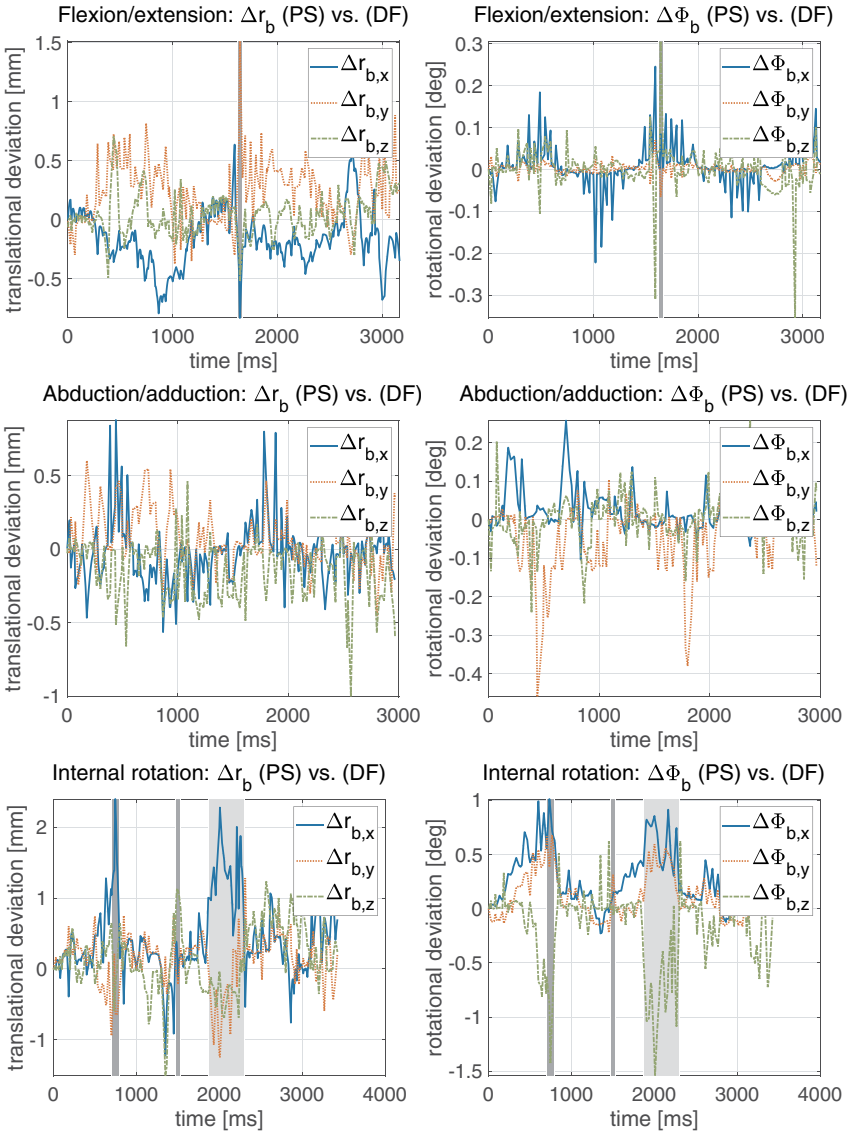

Figure 5.20: Translational (left) and rotational deviations (right) between pressure sensor (PS) and dual fluoroscopy system (DF) after manual fine tuning.

Table 5.2: Root mean square deviations (RMSD) between pressure sensor and dual fluoroscopy system after manual fine tuning.

Movement pattern	RMSD [mm]			RMSD [deg]		
	$\Delta r_{b,x}$	$\Delta r_{b,y}$	$\Delta r_{b,z}$	$\Delta\Phi_{b,x}$	$\Delta\Phi_{b,y}$	$\Delta\Phi_{b,z}$
Flexion/extension	0.05	0.01	0.04	0.28	0.32	0.18
Abduction/adduction	0.05	0.10	0.06	0.19	0.21	0.23
Internal rotation	0.38	0.22	0.36	0.65	0.36	0.45

1° in rotation, which is less than any typically used non-invasive and radiation free method presented yet. In comparison, Anderst et al. [5] showed that the accuracy of dynamic model based dual fluoroscopy tracking with respect to bone-inserted tantalum beads was 0.3 mm to 0.7 mm in translation and 0.3° to 0.9° in rotation. This seems to indicate that the presented pressure foil tracking method is of comparable precision to current dual fluoroscopy bone tracking. Some outliers were verified indicating noise effects which could be filtered by future postprocessing.

Furthermore, manual 2D-3D registration turned out to be difficult and time consuming with currently available tools such as e. g. *JointTrack Biplane*, where rotations can only be executed using EULER angles. The problem of rotational nonlinearity in manual registration is well-known. The only way to circumvent this is to find a proper initial guess such that remaining rotational corrections are very small, and therefore nearly commutative. The pressure sensor system can be seen as a workable method for automatically finding suitable start poses for dual fluoroscopy manual 2D-3D registration, in particular in applications where translations parallel to the X-ray directions and rotations about longitudinal bone axes prevail, which are less visible on the 2D fluoroscopy images.

The optimal solutions of the optimization as well as the resulting residuals show that in real applications residuals of zero are not achievable. The sensitivity analysis of Section **3.3** shows the impact of input errors such as measurement errors on the resulting bone pose. Moreover, the optimization cost function includes the minimal squared distances d_i representing the skin thickness between pressure sensor and bone, which generally are a few millimeters thick.

5.3 Influence factors of manual 2D-3D registration

The influence factors of the model based 2D-3D registration were investigated further in the bachelor thesis of Liang [42]. Dual fluoroscopy images from flexion/extension motion were repetitively registered 7 times by the same rater. Poses of the bone fixed frame $\mathcal{K}_{\mathrm{DF}}$ generated with *JoinTrack Biplane* were then compared, the origin of $\mathcal{K}_{\mathrm{DF}}$ lying close to the centroid of the 3D CT bone surface area. In the first experiment, the image sequence was registered three times on a full HD 14 inch display. It was pointed out that the registration time decreases significantly (from 5 days for the first trial to 2 days for the third trial) for experienced raters. This is due to the fact that there was a learning curve in understanding the effect of executed EULER angle increments in *JointTrack Biplane* on the projected 3D CT bone model. Furthermore, the maximum differences across all trials were 3.83 mm to 7.11 mm in translation and 1.61° to 4.13° in rotation.

In a second experiment, again, the same image sequence was registered three times on a full HD 32 inch TV, yielding maximum discrepancies in the same range: 4.01 mm to 8.00 mm in translation and 1.99° to 3.15° in rotation. Thus, it was hypothesized that the nonlinearity of EULER angles has a bigger impact on the quality of a registered image than pixel size.

Finally, in a third experiment, registration was performed once using the pressure sensor results as starting pose. Again, registration time could be decreased considerably from approximately 2 days to less than a day by means of the initial guess. Moreover, the dimensionless squared jerk measure published by Hogen and Sternad [33] was computed for all resulting poses in the bachelor thesis, showing that a suitable and smooth initial guess results in smoother registered bone pose curves.

5.4 Point-approximated bone model validation

5.4.1 Materials and Methods

The point-approximated bone model introduced in Chapter **4** was used to determine bone poses based on the same measurement data of Section **5.2**. The purpose is to validate this model by identifying bone pose deviations between point- and ellipsoid-approximated bone model. Moreover, the rotations about the sensors' in-plane orthonormal vectors $\underline{u}_{xi}$ and $\underline{u}_{yi}$ were computed with respect to the bone fixed frame $\mathcal{K}_b$

for all three movement patterns, and the corresponding changes of the pressure point due to relative rolling of pressure plane with respect to the contact face were computed.

Rigid body parameters were computed according to Section **4.2** assuming a constant minimal distance $d_i = 1.0$ mm and semi principal axes $a_i = b_i = c_i = 1.0$ μm, where $i = 1, \ldots, 3$. Optimization was performed using the routine `e04unc` of the *Numerical Algorithms Group C library* [71] where all options (i. e. tolerances, step limits, etc.) were left in its default settings. Weighting factors of the cost function Eq. (3.9) where chosen as $\psi_1 = \psi_2 = \psi_3 = 1.0$. Time intervals with erroneous marker and pressure sensor data during flexion/extension and internal rotation were again excluded from evaluation, in particular for the rigid body parameter approximation.

5.4.2 Results

Fig. 5.21 shows the differences between pressure sensor system with point- versus ellipsoid-approximated bone model. Maximum deviations between both approaches are approximately 0.6 mm, 0.4 mm, 0.4 mm in translation and 0.05°, 0.2°, 0.1° in rotation for flexion/extension, abduction/adduction and internal rotation, respectively.

Furthermore, Fig. 5.22 shows the resulting optimal solution of the optimization cost function for all three motions. All residuals are separately illustrated in the Appendix in Fig. C.3.1 to Fig. C.3.3. One can see that, apart from outliers, optimal solutions are in the range of 0.0 mm^2 to 0.2 mm^2 for flexion/extension and abduction/adduction, and 0.0 mm^2 to 0.8 mm^2 for internal rotation.

The results of relative transverse pressure plane rotation with respect to the bone are displayed in Fig. 5.23. It can be seen that the transverse rotations remain at a very low value of $\pm 1.5°$ for flexion/extension and abduction/adduction as well as $\pm 3°$ for internal rotation. Multiplying these angles with the corresponding curvature radius of the contact face gives variations of the contact point due to relative transverse rotation of the contact plane in the range of ± 0.3 mm for flexion/extension and abduction/adduction as well as ± 0.5 mm for internal rotation (see Fig. 5.24).

5.4.3 Discussion

The results point out that the approximation of contact relevant bone regions by means of points instead of ellipsoids had only small effects on the resulting relative bone

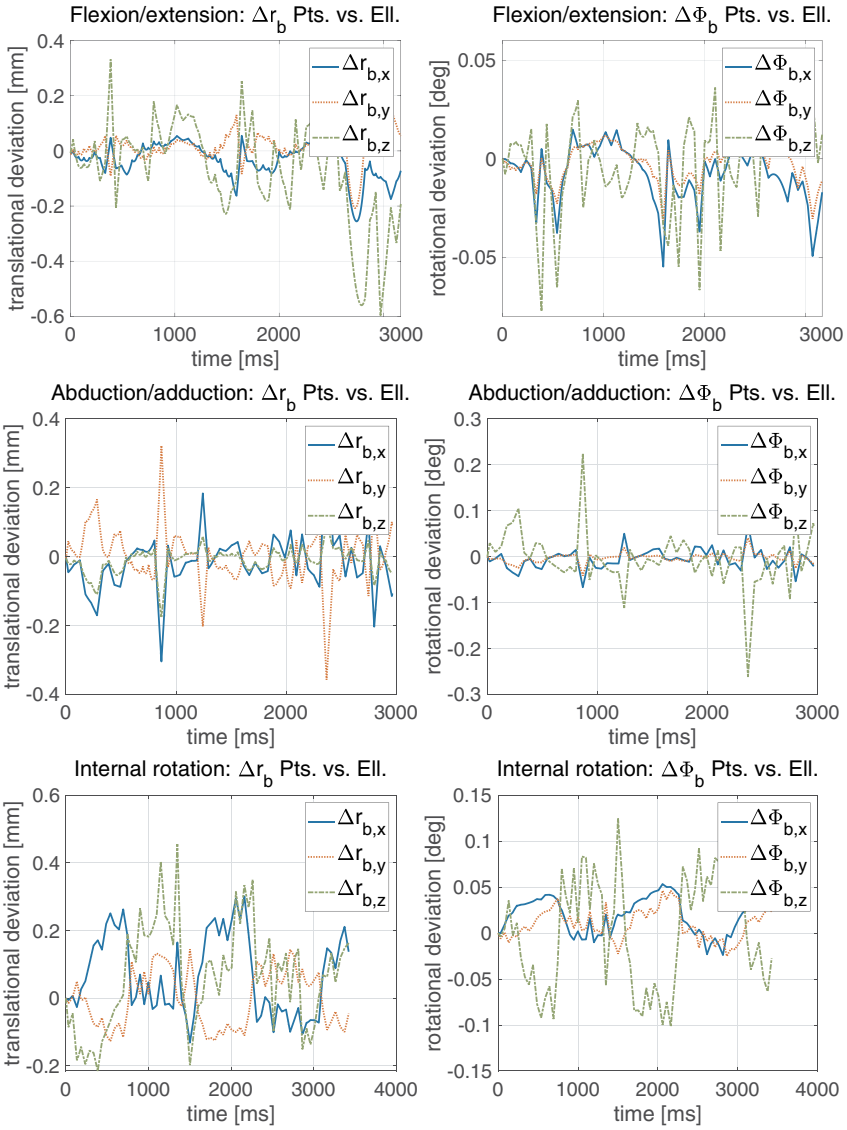

Figure 5.21: Translational (left) and rotational deviations (right) between pressure sensor system using the point- and ellipsoid-approximated bone model.

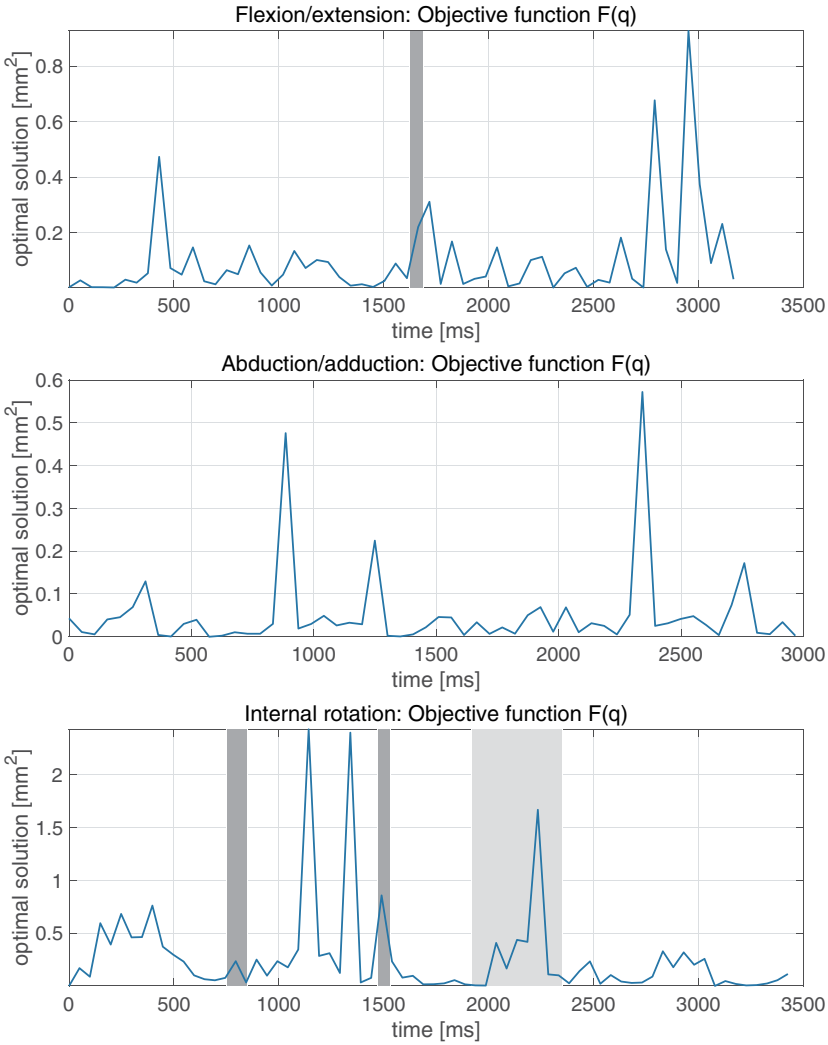

Figure 5.22: Optimal solutions found by the *NAG* optimizer for the point-approximated bone model.

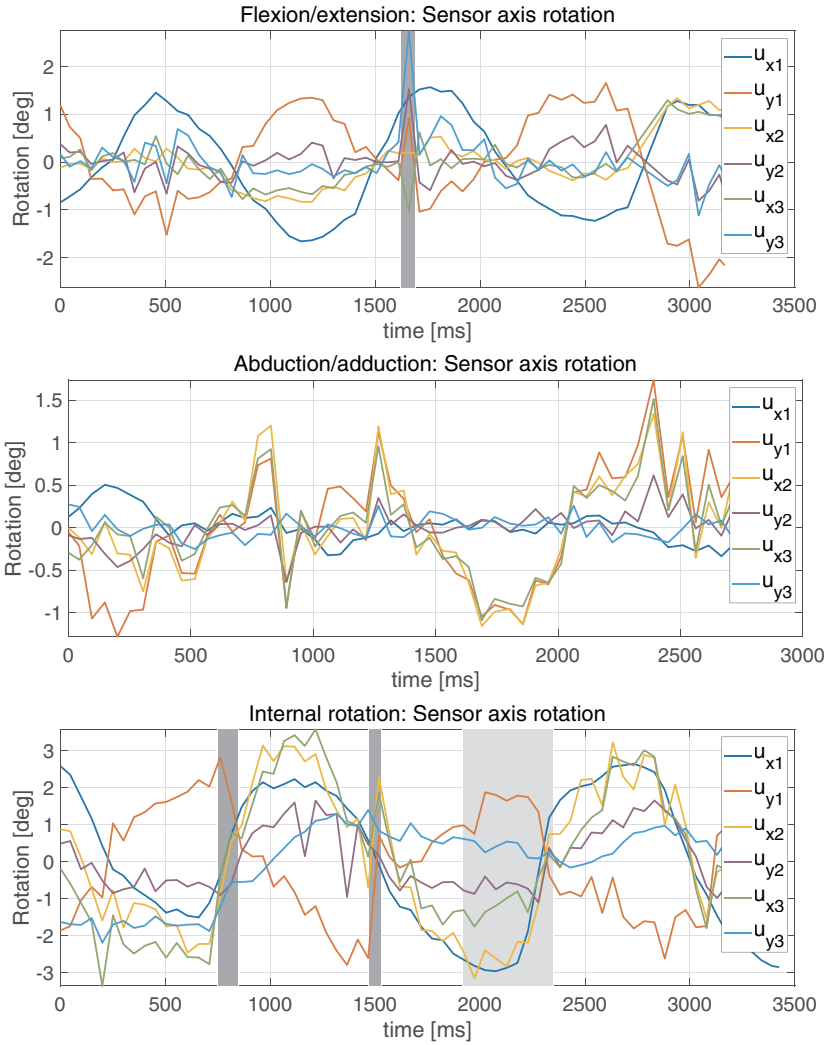

Figure 5.23: Estimated relative rotations about the sensors' in-plane orthonormal vectors $\underline{u}_{xi}$ and $\underline{u}_{yi}$ with respect to the bone fixed frame $\mathcal{K}_b$. (Indexing: 1 $\widehat{=}$ tuberosity, 2 $\widehat{=}$ lateral malleolus and 3 $\widehat{=}$ medial malleolus).

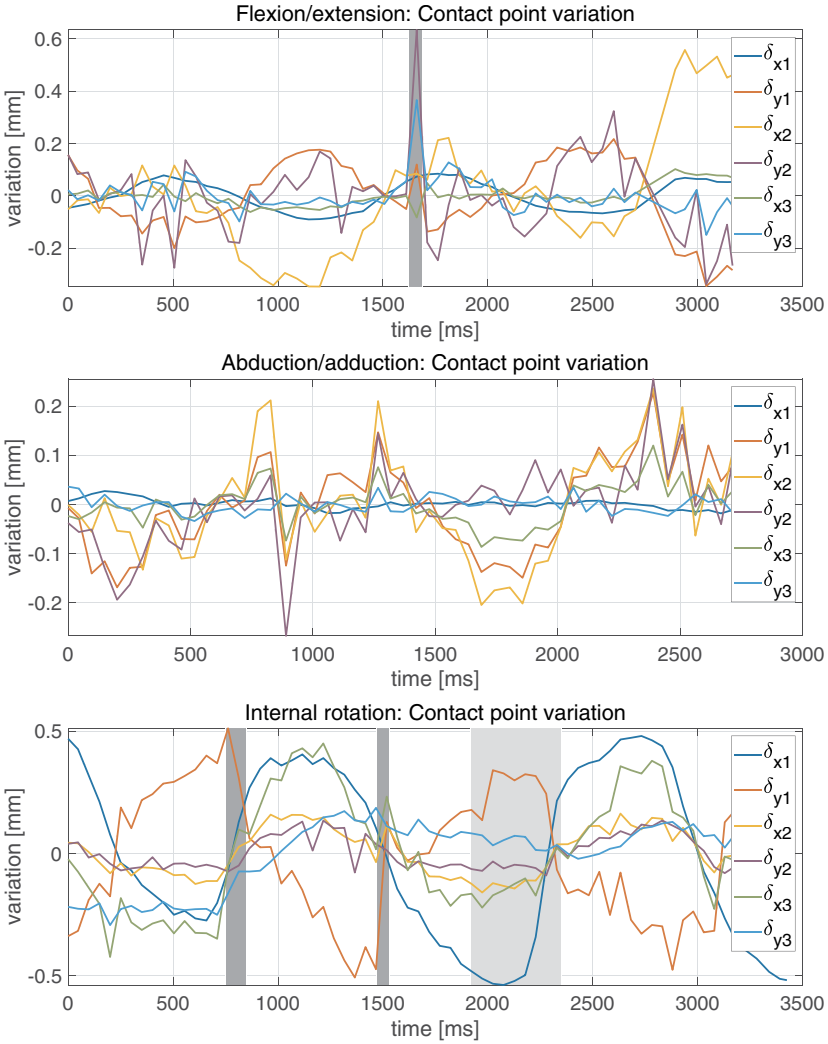

Figure 5.24: Estimated variations of the contact point due to relative transverse rotations of the pressure sensor planes. (Indexing: 1 $\widehat{=}$ tuberosity, 2 $\widehat{=}$ lateral malleolus and 3 $\widehat{=}$ medial malleolus).

motion, even for the case of internal rotation, where larger relative rotations between pressure sensor and bone surface occurred. As expected, the largest relative rotations of $\pm 3^\circ$ between sensors and bone were found during internal rotation motion being approximately twice as high as for the other motion tasks. However, for the present case, variations of the contact point stay below 0.5 mm for all movement patterns, which is less than the pressure sensors' grid resolution suggesting that in real applications, model errors due to the point approximation can be neglected to first order.

In comparison to the ellipsoid-approximated bone model, optimal solutions by the point-approximated model were improved by a factor of 10 for flexion/extension and abduction/adduction, and remained unchanged for internal rotation motion.

6 Conclusions and outlook

6.1 Conclusions

This thesis shows that non-invasive and, at the same time, accurate 3D bone pose tracking is possible by external pressure sensor palpation. To this end, the problem was first regarded in 2D, showing similarities to the 3PPR parallel manipulator, which is known from the literature to have always two real solutions. However, in the case of three ellipse contacts, a maximum number of 32 different real solutions could be obtained for a given symmetric case. Additionally, it is shown that each pose of any symmetric configuration must occur in pairs, both having the same position of the rigid body center, but oriented differently. In generalization of this, 64 solutions for a general case could be obtained, whereas the maximum number of real solutions found so far was 48. It was found that different solutions might yield poses that are very close to each other, leading to a poorly-conditioned numerical behavior for root finding. Interestingly, by using tangent points as additional dependent variables and, moreover, the additional condition that each tangent point must face the corresponding line, the solution variety can be reduced significantly. At the same time, a good separation of multiple solutions can be achieved.

Subsequently, the mathematical model could successfully be extended to 3D by the derivation of 12 constraint equations. The bone pose determination by optimization turned out to be feasible and rather insensitive toward small variations in its input parameters. By including the squared minimal distances between pressure sensors and ellipsoids in the optimization cost function, input errors were much less amplified, thus yielding a better convergence of the optimizer.

The validation of the approach shows that, for in-vivo measurements of the shank, root mean square errors below 0.05 mm and 0.32° for flexion/extension, 0.10 mm and 0.23° for abduction/adduction, and 0.38 mm and 0.65° for internal rotation can be achieved. To the authors' knowledge, this is less than any non-invasive and radiation-free method presented yet.

Finally, the point-approximated bone model technique that was first introduced in this thesis makes this approach universally applicable, as it is automatable and independent of computed tomography scans. At the same time, it reduces the amount of data to be surveyed for the bone tracking. The validation shows that deviations between point- and ellipsoid-approximated bone model are rather small, namely 0.6 mm and 0.05°

for flexion/extension, 0.4 mm and 0.2° for abduction/adduction, and 0.4 mm and 0.1° for internal rotation (for translation and rotation respectively). This shows that the simple point-tracking can lead to as good tracking results as the more complex ellipsoid-tracking method when relative rotations between pressure sensors and underlying bones are small.

6.2 Outlook

From the results in this thesis, it is likely that a suitable initial pose has the most significant influence on the accuracy of dual fluoroscopy manual 2D-3D registration. For this reason, the external pressure sensor approach could be further developed as a tool for determining these poses. Furthermore, the author suggests that presented procedures may partially be of interest for similar applications such as bone pose tracking techniques using ultrasound transducers, e. g. in order to circumvent the necessity of a bone model from a computed tomography scan.

While the method is very promising and validated, there are a number of issues to be tackled in the future. The attachment of the pressure sensors on the skin can be optimized such that retro-reflective markers always remain inside the cameras field of view. Likewise, it should be guaranteed that the bone protuberance stays in contact with the pressure sensor during the entire measurement. Moreover, further numerical tests would be valuable to determine optimal weighting factors for the combination of precision and feasibility of the optimization cost function. Finally, tests for application to other bone segments would be of interest.

Appendices

A Geometrical problem analysis for the planar case

A.1 General solutions

Table A.1.1: Numerical solutions for all 48 real solutions shown in Fig. A.1.1 and Fig. A.1.2.

Sol. no.	Rigid body pose			Sol. no.	Rigid body pose		
i	x_b	y_b	φ_b [deg]	i	x_b	y_b	φ_b [deg]
1	7.282	7.673	-6.808	25	7.388	16.795	123.588
2	6.911	7.224	-3.383	26	10.781	17.507	-118.587
3	12.551	7.224	-54.171	27	11.400	16.798	-125.177
4	6.677	7.914	-6.247	28	1.700	4.258	-49.426
5	6.328	7.674	-3.971	29	2.905	7.957	91.590
6	11.362	15.196	-67.881	30	1.392	6.373	89.431
7	9.354	11.641	-85.010	31	3.221	10.826	93.873
8	9.842	14.476	-81.198	32	8.817	9.872	38.338
9	7.014	9.583	-87.825	33	5.447	5.799	-5.161
10	2.656	8.252	-130.989	34	5.482	5.825	-4.790
11	5.361	14.039	175.542	35	1.150	8.479	91.200
12	5.419	14.154	174.347	36	3.241	8.387	94.014
13	6.796	11.661	-86.251	37	4.842	6.118	-5.401
14	8.889	11.529	-88.512	38	4.877	6.189	-4.666
15	4.783	14.436	175.039	39	7.524	11.876	47.753
16	4.791	14.442	174.950	40	3.021	10.479	92.427
17	1.367	10.223	-140.270	41	0.004	5.434	100.038
18	6.724	9.080	-85.732	42	0.593	8.345	95.395
19	8.654	13.662	-90.238	43	1.068	4.913	109.313
20	7.043	11.977	-88.034	44	3.888	12.552	175.818
21	8.465	15.996	131.886	45	3.611	12.362	174.012
22	-1.248	3.398	56.532	46	2.422	6.998	124.062
23	-0.660	2.772	62.603	47	3.313	12.995	176.388
24	2.827	3.467	-58.008	48	2.994	12.610	173.452

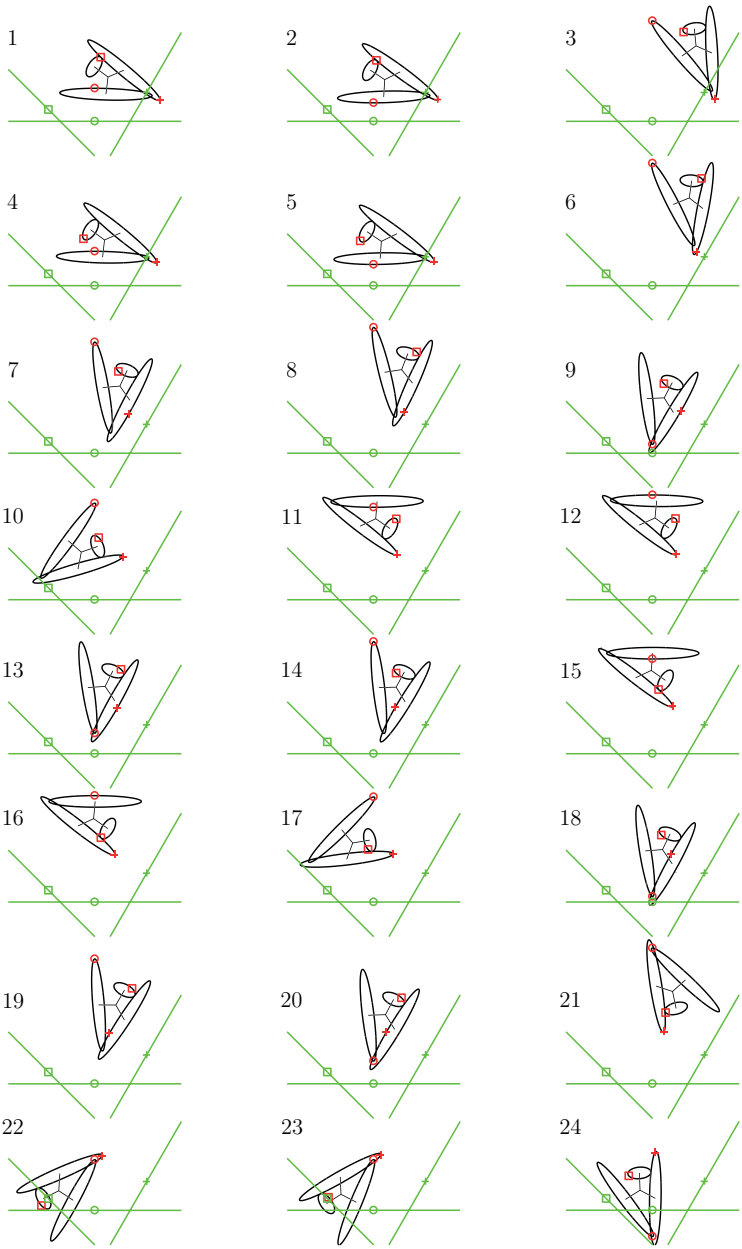

Figure A.1.1: Part1: 48 real solutions for the general set of parameters of Table 2.2.

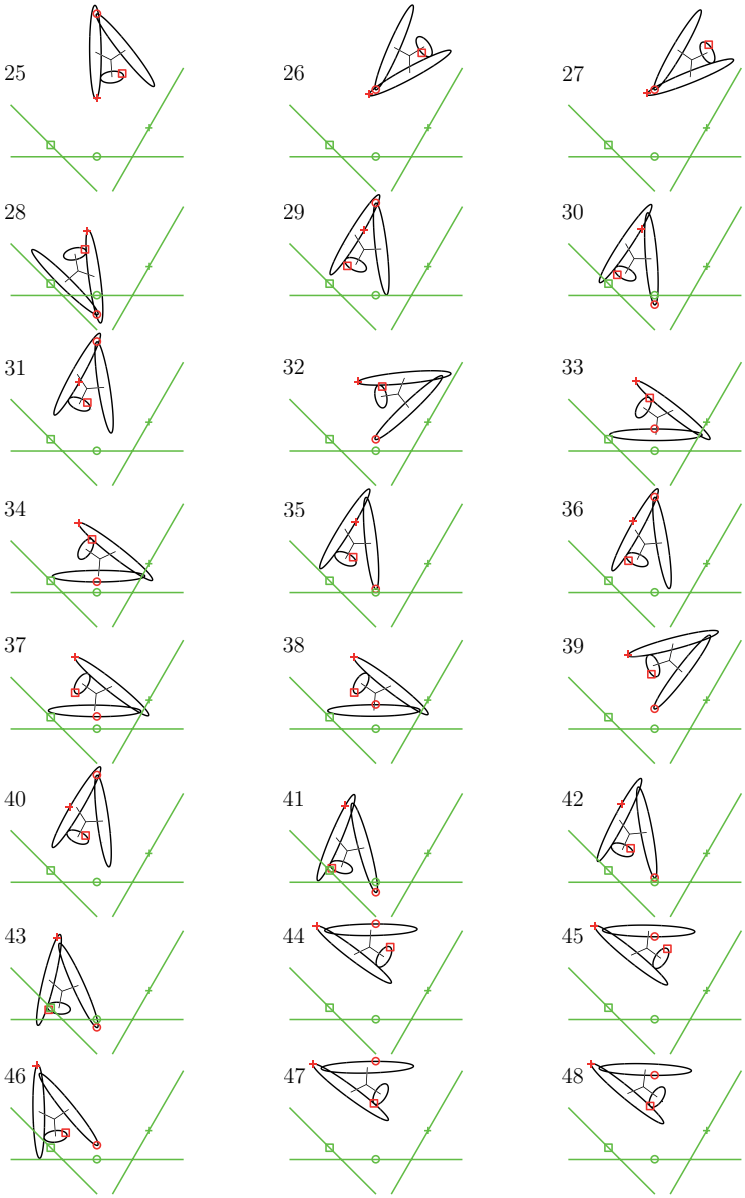

Figure A.1.2: Part2: 48 real solutions for the general set of parameters of Table 2.2.

B 3D pose estimation based on the ellipsoid-approximated bone model

B.1 Reference pose for sensitivity analysis

Table B.1.1: Sensor poses. (Indexing: 1 $\widehat{=}$ tuberosity, 2 $\widehat{=}$ lateral malleolus and 3 $\widehat{=}$ medial malleolus.)

Index	Sensor poses	
i	$\underline{r}_{\mathcal{P}_i,\mathrm{ref}}$ [mm]	$\mathbf{R}_{\mathcal{P}_i,\mathrm{ref}}$
1	$\begin{bmatrix} 1.03 \\ 173.30 \\ 11.54 \end{bmatrix}$	$\begin{bmatrix} 0.606852 & 0.267269 & 0.748531 \\ -0.002635 & 0.942439 & -0.334369 \\ -0.794810 & 0.200940 & 0.572625 \end{bmatrix}$
2	$\begin{bmatrix} 37.40 \\ -184.68 \\ 2.08 \end{bmatrix}$	$\begin{bmatrix} -0.040443 & 0.511988 & 0.858040 \\ 0.994995 & -0.057895 & 0.081444 \\ 0.091375 & 0.857039 & -0.507084 \end{bmatrix}$
3	$\begin{bmatrix} -31.39 \\ -166.96 \\ -4.14 \end{bmatrix}$	$\begin{bmatrix} 0.113945 & 0.249617 & -0.961617 \\ 0.745604 & 0.618193 & 0.248820 \\ 0.656575 & -0.745338 & -0.115675 \end{bmatrix}$

Table B.1.2: Ellipsoid parameters. (Indexing: 1 $\widehat{=}$ tuberosity, 2 $\widehat{=}$ lateral malleolus and 3 $\widehat{=}$ medial malleolus.)

Index	Offsets	Semi principal axes
i	$\Delta\bar{r}_{i,\mathrm{ref}}$ [mm]	$\{a_i\,,b_i\,,c_i\}_{\mathrm{ref}}$ [mm]
1	$[\,-8.74\,,\ \ 177.12\,,\ \ 11.34]^{\mathrm{T}}$	$\{6.06\,,9.52\,,12.01\}$
2	$[\ \ 35.02\,,-183.42\,,\ \ 4.49]^{\mathrm{T}}$	$\{3.06\,,8.58\,,\ \ 5.96\}$
3	$[-27.32\,,-167.64\,,-3.89]^{\mathrm{T}}$	$\{4.13\,,3.66\,,\ \ 5.58\}$

Table B.1.3: Initial rigid body pose and relative pressure point coordinates.

Rigid body pose		Pressure point position		
$\underline{r}_{b,\mathrm{ref}}$ [mm]	$\mathbf{R}_{b,\mathrm{ref}}$	${}_{\mathcal{P}_1}\underline{r}_{p1,\mathrm{ref}}$ [mm]	${}_{\mathcal{P}_2}\underline{r}_{p2,\mathrm{ref}}$ [mm]	${}_{\mathcal{P}_3}\underline{r}_{p3,\mathrm{ref}}$ [mm]
$\underline{0}$	Identity matrix	$\underline{0}$	$\underline{0}$	$\underline{0}$

C Validation

C.1 Calibration Pencil

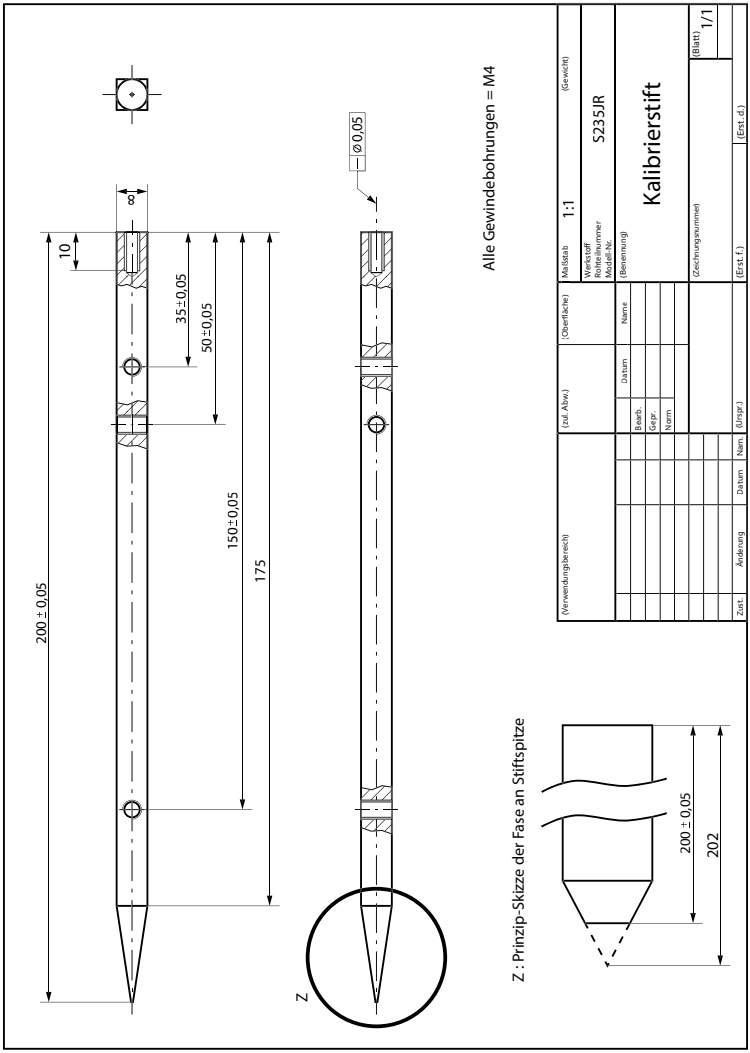

Figure C.1.1: Technical drawing of the calibration pencil.

C.2 Residuals - ellipsoid-approximated bone model

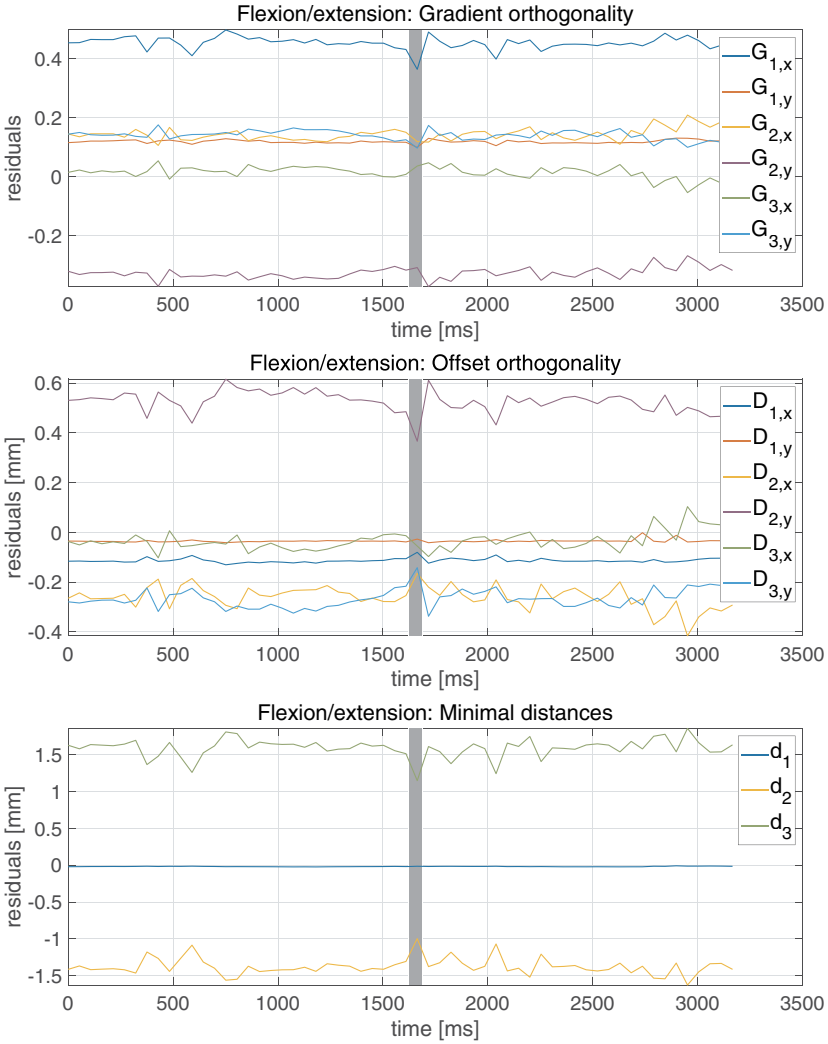

Figure C.2.1: Residuals of the optimization cost function for flexion/extension motion (ellipsoid-approximated bone model). (Indexing: 1 $\widehat{=}$ tuberosity, 2 $\widehat{=}$ lateral malleolus and 3 $\widehat{=}$ medial malleolus.)

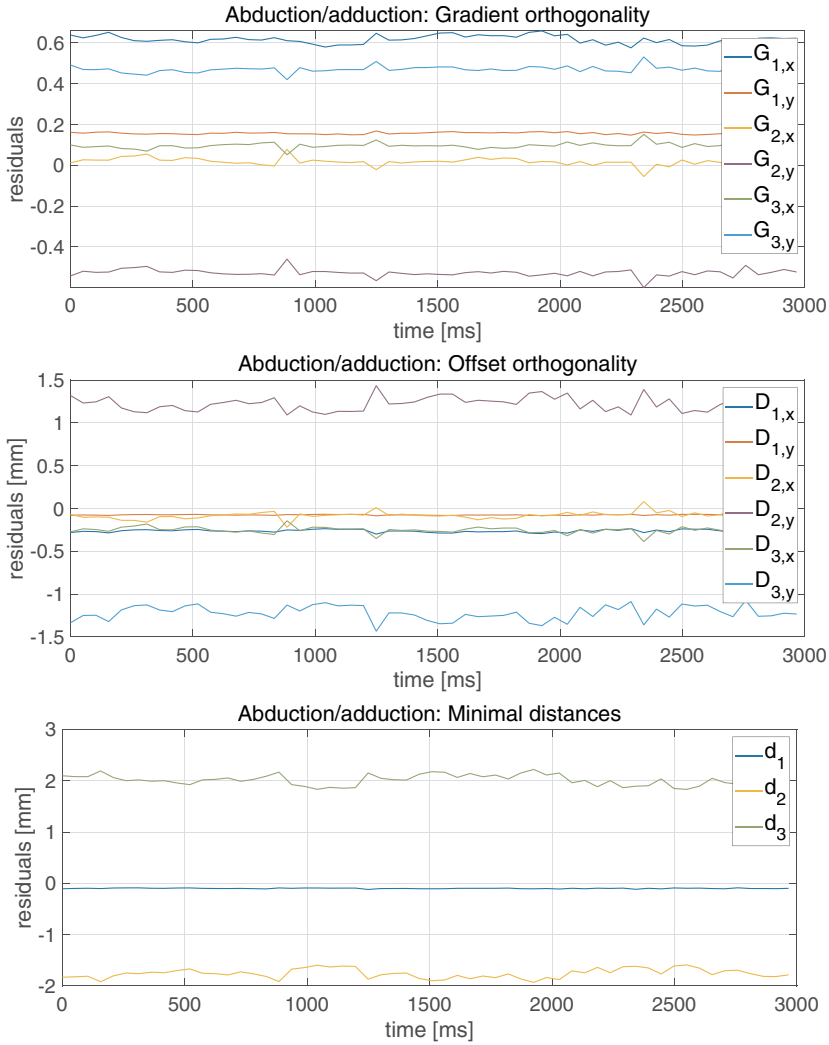

Figure C.2.2: Residuals of the optimization cost function for abduction/adduction motion (ellipsoid-approximated bone model). (Indexing: 1 $\widehat{=}$ tuberosity, 2 $\widehat{=}$ lateral malleolus and 3 $\widehat{=}$ medial malleolus.)

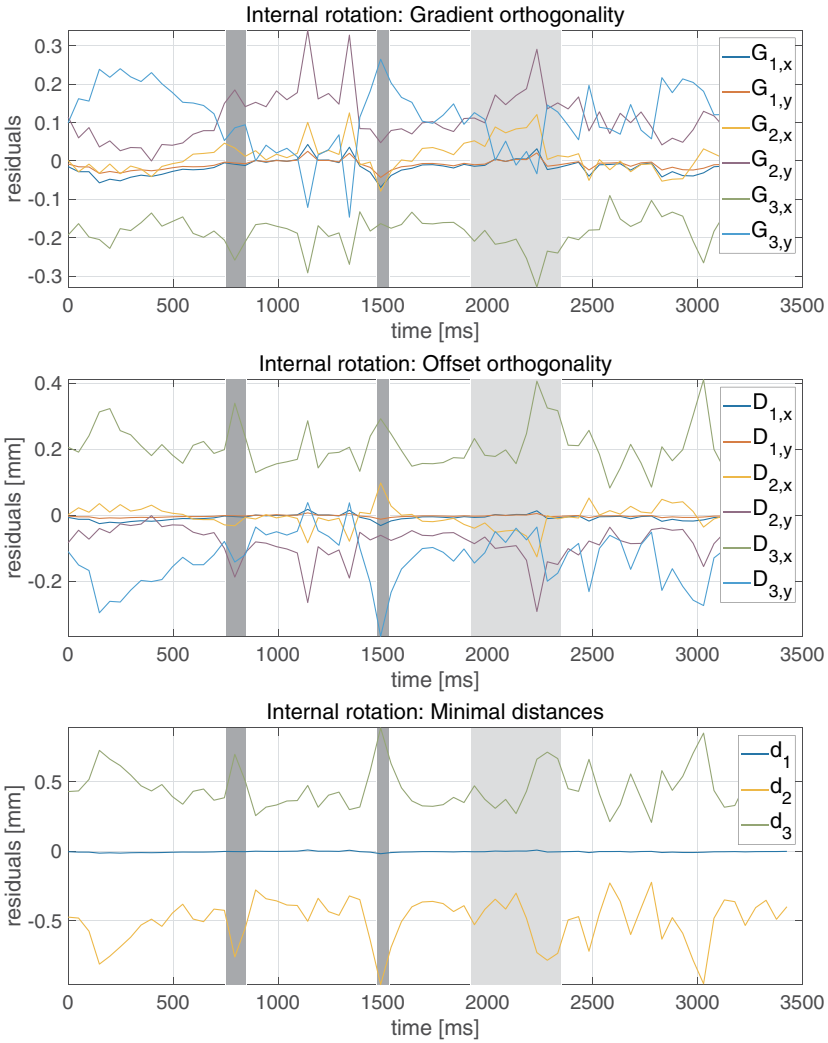

Figure C.2.3: Residuals of the optimization cost function for internal rotation motion (ellipsoid-approximated bone model). (Indexing: 1 $\widehat{=}$ tuberosity, 2 $\widehat{=}$ lateral malleolus and 3 $\widehat{=}$ medial malleolus.)

C.3 Residuals - point-approximated bone model

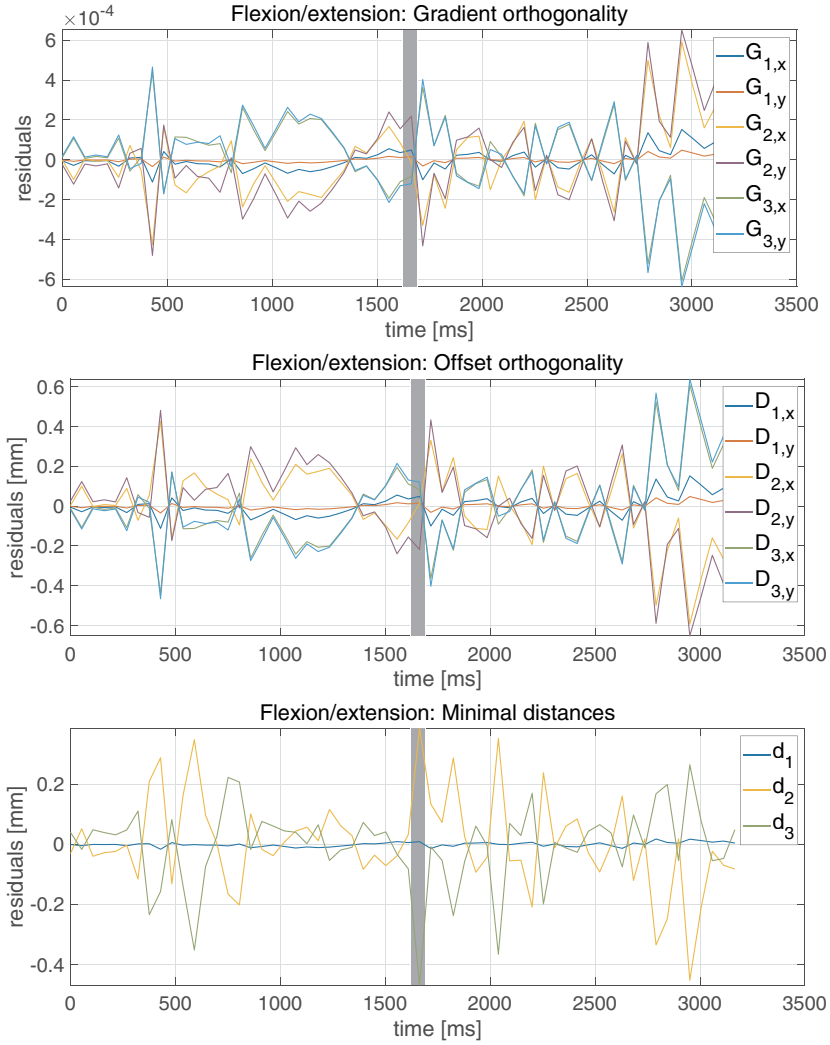

Figure C.3.1: Residuals of the optimization cost function for flexion/extension motion (point-approximated bone model). (Indexing: 1 $\widehat{=}$ tuberosity, 2 $\widehat{=}$ lateral malleolus and 3 $\widehat{=}$ medial malleolus.)

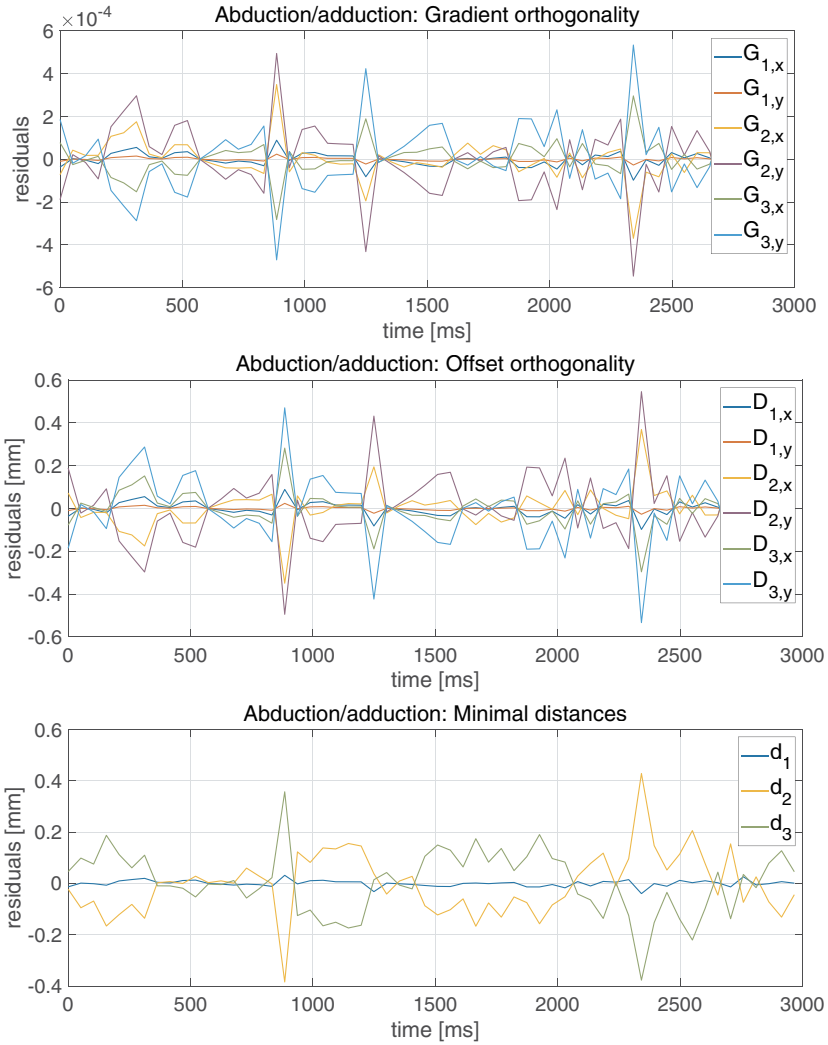

Figure C.3.2: Residuals of the optimization cost function for abduction/adduction motion (point-approximated bone model). (Indexing: 1 $\widehat{=}$ tuberosity, 2 $\widehat{=}$ lateral malleolus and 3 $\widehat{=}$ medial malleolus.)

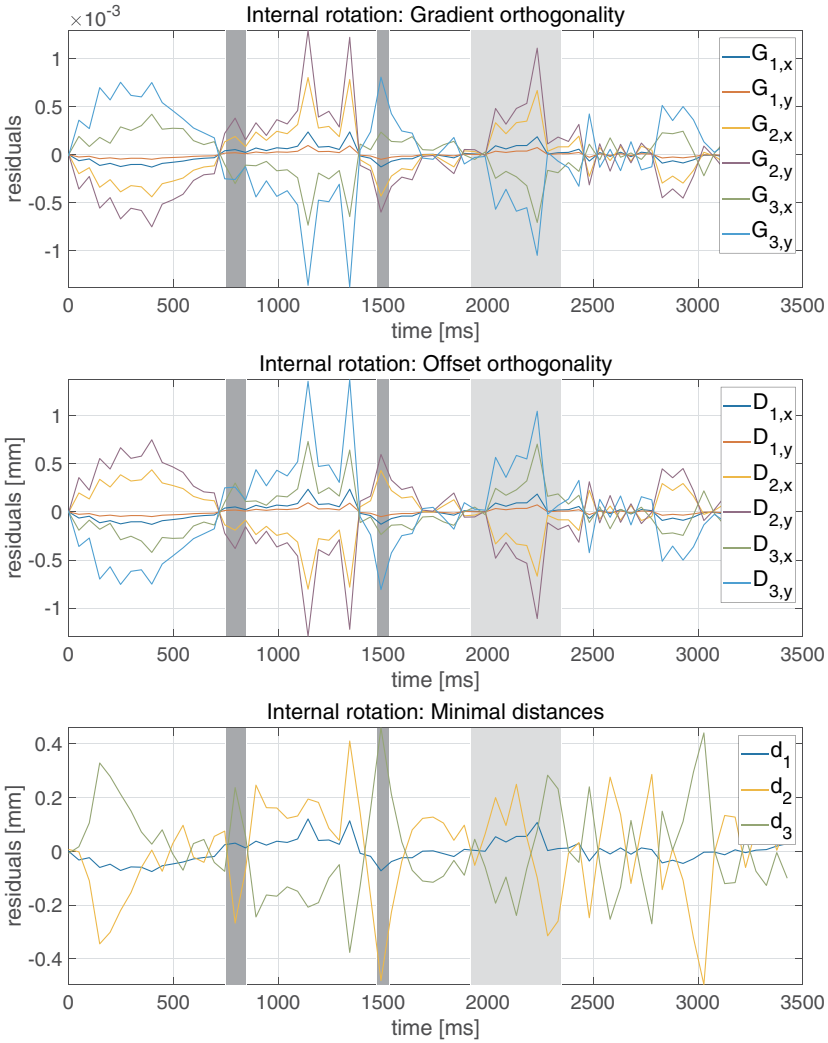

Figure C.3.3: Residuals of the optimization cost function for internal rotation motion (point-approximated bone model). (Indexing: 1 $\widehat{=}$ tuberosity, 2 $\widehat{=}$ lateral malleolus and 3 $\widehat{=}$ medial malleolus.)

C.4 Parameters - ellipsoid-approximated bone model

Table C.4.1: Rigid body parameters with respect to the bone fixed frame $\mathcal{K}_b$ for flexion/extension and abduction/adduction motion.

	Semi-axes [mm]			Cardan xyz [deg]			Offsets [mm]		
Ellipsoid	a	b	c	α	β	γ	$\Delta\bar{r}_x$	$\Delta\bar{r}_y$	$\Delta\bar{r}_z$
Tuberosity	6.1	9.5	12.0	-59.8	-56.7	68.6	-8.7	177.1	11.3
Lateral malleolus	3.1	8.6	6.0	4.6	25.4	6.8	35.0	-183.4	4.5
Medial malleolus	4.1	3.7	5.6	19.8	-17.3	5.6	-27.3	-167.6	-3.9

Table C.4.2: Rigid body parameters with respect to the bone fixed frame $\mathcal{K}_b$ for internal rotation motion.

	Semi-axes [mm]			Cardan xyz [deg]			Offsets [mm]		
Ellipsoid	a	b	c	α	β	γ	$\Delta\bar{r}_x$	$\Delta\bar{r}_y$	$\Delta\bar{r}_z$
Tuberosity	2.5	5.1	2.5	0.0	0.0	0.0	0.0	176.8	1.3
Lateral malleolus	1.8	2.9	2.9	0.0	18.5	0.0	31.2	-180.1	0.3
Medial malleolus	1.7	3.5	1.6	0.0	0.0	0.0	-30.7	-173.5	0.0

C.5 Parameters - point-approximated bone model

Table C.5.1: Averaged rigid body parameters from self-adjusting parameter approximation. (Indexing: 1 $\widehat{=}$ tuberosity, 2 $\widehat{=}$ lateral malleolus and 3 $\widehat{=}$ medial malleolus.)

Movement pattern	Averaged rigid body parameters		
	$\Delta\underline{\bar{r}}_1$ [mm]	$\Delta\underline{\bar{r}}_2$ [mm]	$\Delta\underline{\bar{r}}_3$ [mm]
Flexion/extension	$\begin{bmatrix} 0.0 \\ 177.8 \\ 0.0 \end{bmatrix}$	$\begin{bmatrix} 36.0 \\ -184.0 \\ 0.0 \end{bmatrix}$	$\begin{bmatrix} -36.0 \\ -171.6 \\ 0.0 \end{bmatrix}$
Abduction/adduction	$\begin{bmatrix} 0.0 \\ 177.9 \\ 0.0 \end{bmatrix}$	$\begin{bmatrix} 35.1 \\ -180.1 \\ 0.0 \end{bmatrix}$	$\begin{bmatrix} -35.1 \\ -175.8 \\ 0.0 \end{bmatrix}$
Internal rotation	$\begin{bmatrix} 0.0 \\ 176.7 \\ 0.0 \end{bmatrix}$	$\begin{bmatrix} 32.3 \\ -180.0 \\ 0.0 \end{bmatrix}$	$\begin{bmatrix} -32.3 \\ -173.4 \\ 0.0 \end{bmatrix}$

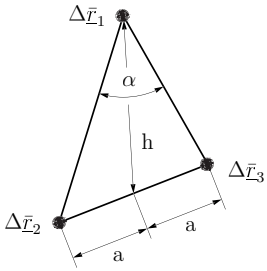

Figure C.5.1: Representation of the characteristic lengths and angle of a rigid body point model for the description of Fig. C.5.2. (Indexing: 1 $\widehat{=}$ tuberosity, 2 $\widehat{=}$ lateral malleolus and 3 $\widehat{=}$ medial malleolus.)

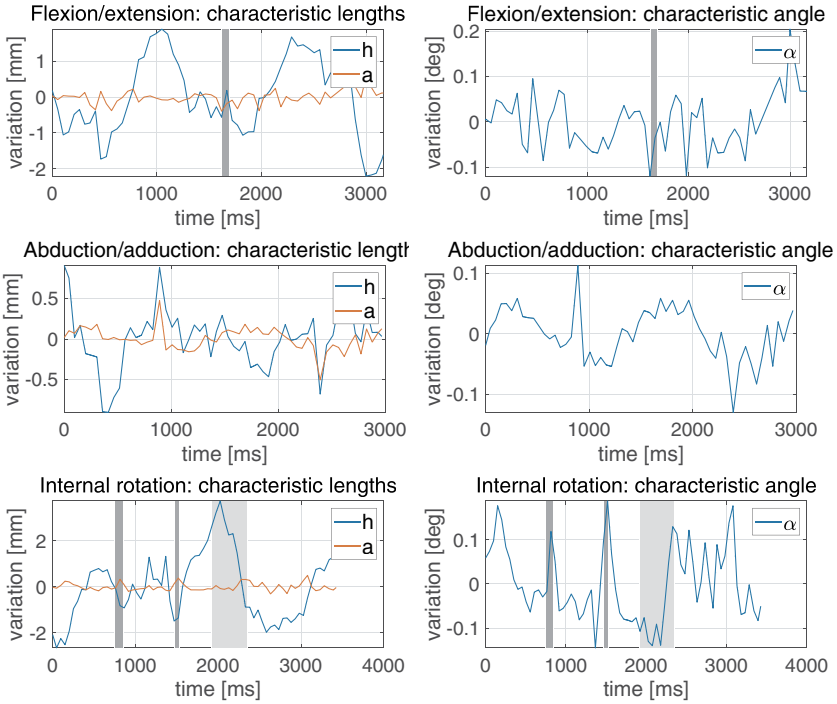

Figure C.5.2: Variations of the characteristic lengths and angle according to Fig. C.5.1 during self-adjusting parameter approximation. Large h-displacements result due to the line-coordinate DOF λ, which is however eliminated in the bone-pose fitting.

Bibliography

[1] The webplatform of ART. `http://www.ar-tracking.com/home/`. Accessed: 2019-04-03.

[2] M. Akbarshahi, A. G. Schache, J. W. Fernandez, R. Baker, S. Banks, and M. G. Pandy. Non-invasive assessment of soft-tissue artifact and its effect on knee joint kinematics during functional activity. *Journal of Biomechanics*, 43(7):1292 – 1301, 2010.

[3] E. J. Alexander and T. P. Andriacchi. Correcting for deformation in skin-based marker systems. *Journal of Biomechanics*, 34(3):355 – 361, 2001.

[4] M. S. Andersen, D. L. Benoit, M. Damsgaard, D. K. Ramsey, and J. Rasmussen. Do kinematic models reduce the effects of soft tissue artefacts in skin marker-based motion analysis? An in vivo study of knee kinematics. *Journal of Biomechanics*, 43(2):268–273, 2010.

[5] W. Anderst, R. Zauel, J. Bishop, E. Demps, and S. Tashman. Validation of three-dimensional model-based tibio-femoral tracking during running. *Medical Engineering & Physics*, 31(1):10 – 16, 2009.

[6] S. A. Banks and W. A. Hodge. Accurate measurement of three-dimensional knee replacement kinematics using single-plane fluoroscopy. *IEEE Transactions on Biomedical Engineering*, 43(6):638–649, 1996.

[7] E. Berthonnaud, G. Herzberg, K. D. Zhao, K. N. An, and J. Dimnet. Three-dimensional in vivo displacements of the shoulder complex from biplanar radiography. *Surgical and Radiologic Anatomy*, 27(3):214–222, Aug 2005.

[8] M. J. Bey, R. Zauel, S. K. Brock, and S. Tashman. Validation of a new model-based tracking technique for measuring three-dimensional, in vivo glenohumeral joint kinematics. *Journal of Biomechanical Engineering*, 128(4):604–609, 2006.

[9] J. Bingham and G. Li. An optimized image matching method for determining in-vivo TKA kinematics with a dual-orthogonal fluoroscopic imaging system. *Journal of Biomechanical Engineering*, 128(4):588–595, 2006.

[10] B. Bonnechere, B. Jansen, P. Salvia, H. Bouzahouene, L. Omelina, F. Moiseev, V. Sholukha, J. Cornelis, M. Rooze, and S. V. S. Jan. Validity and reliability of the Kinect within functional assessment activities: Comparison with standard stereophotogrammetry. *Gait & Posture*, 39(1):593–598, 2014.

[11] G. Bradski. The OpenCV Library. *Dr. Dobb's Journal of Software Tools*, 2000.

[12] E. L. Brainerd, D. B. Baier, S. M. Gatesy, T. L. Hedrick, K. A. Metzger, S. L. Gilbert, and J. J. Crisco. X-ray reconstruction of moving morphology (XROMM): Precision, accuracy and applications in comparative biomechanics research. *Journal of Experimental Zoology Part A: Ecological Genetics and Physiology*, 313A(5):262–279, 2010.

[13] A. Cappello, A. Cappozzo, P. F. L. Palombara, L. Lucchetti, and A. Leardini. Multiple anatomical landmark calibration for optimal bone pose estimation. *Human Movement Science*, 16(2-3):259 – 274, 1997. 3-D Analysis of Human Movement - {II}.

[14] A. Cappello, R. Stagni, S. Fantozzi, and A. Leardini. Soft tissue artifact compensation in knee kinematics by double anatomical landmark calibration: Performance of a novel method during selected motor tasks. *IEEE Transactions on Biomedical Engineering*, 52(6):992–998, 2005.

[15] A. Cappozzo, F. Catani, A. Leardini, M. Benedetti, and U. D. Croce. Position and orientation in space of bones during movement: Experimental artefacts. *Clinical Biomechanics*, 11(2):90 – 100, 1996.

[16] A. Cappozzo, U. D. Croce, A. Leardini, and L. Chiari. Human movement analysis using stereophotogrammetry: Part 1: Theoretical background. *Gait & Posture*, 21(2):186 – 196, 2005.

[17] C. Chen, W. J. Heyne, and D. Jackson. A new 6-dof 3-legged parallel mechanism for force-feedback interface. In *Mechatronics and Embedded Systems and Applications (MESA), 2010 IEEE/ASME International Conference on*, pages 539–544. IEEE, July 2010.

[18] P. L. Chin, K. Y. Yang, S. J. Yeo, and N. N. Lo. Randomized control trial comparing radiographic total knee arthroplasty implant placement using computer navigation versus conventional technique. *The Journal of Arthroplasty*, 20(5):618 – 626, 2005.

[19] K.-B. Choi. Kinematic analysis and optimal design of 3-PPR planar parallel manipulator. *KSME International Journal*, 17(4):528–537, 2003.

[20] R. A. Clark, K. J. Bower, B. F. Mentiplay, K. Paterson, and Y.-H. Pua. Concurrent validity of the Microsoft Kinect for assessment of spatiotemporal gait variables. *Journal of Biomechanics*, 46(15):2722–2725, 2013.

[21] D. Cox, J. Little, and D. O'Shea. *Ideals, Varieties, and Algorithms*, volume 3. Springer, 2007.

[22] Y. Ehara, H. Fujimoto, S. Miyazaki, M. Mochimaru, S. Tanaka, and S. Yamamoto. Comparison of the performance of 3D camera systems II. *Gait & Posture*, 5(3):251–255, 1997.

[23] P. Eichelberger, M. Ferraro, U. Minder, T. Denton, A. Blasimann, F. Krause, and H. Baur. Analysis of accuracy in optical motion capture – A protocol for laboratory setup evaluation. *Journal of Biomechanics*, 49(10):2085–2088, 2016.

[24] M. Eltoukhy, J. Oh, C. Kuenze, and J. Signorile. Improved Kinect-based spatiotemporal and kinematic treadmill gait assessment. *Gait & Posture*, 51:77–83, 2017.

[25] A. Ferrari, A. G. Cutti, and A. Cappello. A new formulation of the coefficient of multiple correlation to assess the similarity of waveforms measured synchronously by different motion analysis protocols. *Gait & Posture*, 31(4):540 – 542, 2010.

[26] Y. Fukuoka, A. Hoshino, and A. Ishida. Accurate 3D pose estimation method for polyethylene wear assessment in total knee replacement. In *Engineering in Medicine and Biology Society, 1997. Proceedings of the 19th Annual International Conference of the IEEE*, volume 4, pages 1849–1852. IEEE, 1997.

[27] J. Fuller, L.-J. Liu, M. Murphy, and R. Mann. A comparison of lower-extremity skeletal kinematics measured using skin- and pin-mounted markers. *Human Movement Science*, 16(2-3):219 – 242, 1997. 3-D Analysis of Human Movement - {II}.

[28] B. Galna, G. Barry, D. Jackson, D. Mhiripiri, P. Olivier, and L. Rochester. Accuracy of the Microsoft Kinect sensor for measuring movement in people with Parkinson's disease. *Gait & Posture*, 39(4):1062–1068, 2014.

[29] E. Garling, B. Kaptein, B. Mertens, W. Barendregt, H. Veeger, R. Nelissen, and E. Valstar. Soft-tissue artefact assessment during step-up using fluoroscopy and skin-mounted markers. *Journal of Biomechanics*, 40, Supplement 1:S18 – S24, 2007. Interaction of Mechanics and Biology in Knee Joint Restoration and Regeneration.

[30] E. H. Garling, B. L. Kaptein, K. Geleijns, R. G. Nelissen, and E. R. Valstar. Marker configuration model-based Roentgen fluoroscopic analysis. *Journal of Biomechanics*, 38(4):893 – 901, 2005.

[31] H. A. Gray, S. Guan, and M. G. Pandy. Accuracy of mobile biplane X-ray imaging in measuring 6-degree-of-freedom patellofemoral kinematics during overground gait. *Journal of Biomechanics*, 57:152–156, 2017.

[32] G. R. Hanson, J. F. Suggs, A. A. Freiberg, S. Durbhakula, and G. Li. Investigation of in vivo 6DOF total knee arthoplasty kinematics using a dual orthogonal fluoroscopic system. *Journal of Orthopaedic Research*, 24(5):974–981, 2006.

[33] N. Hogan and D. Sternad. Sensitivity of smoothness measures to movement duration, amplitude, and arrests. *Journal of Motor Behavior*, 41(6):529–534, 2009.

[34] J. P. Holden, J. A. Orsini, K. L. Siegel, T. M. Kepple, L. H. Gerber, and S. J. Stanhope. Surface movement errors in shank kinematics and knee kinetics during gait. *Gait & Posture*, 5(3):217 – 227, 1997.

[35] R. Jia, P. Monk, D. Murray, J. A. Noble, and S. Mellon. CAT & MAUS: A novel system for true dynamic motion measurement of underlying bony structures with compensation for soft tissue movement. *Journal of Biomechanics*, 62:156–164, 2017.

[36] D. Karlsson and R. Tranberg. On skin movement artefact-resonant frequencies of skin markers attached to the leg. *Human Movement Science*, 18(5):627 – 635, 1999.

[37] A. Kecskeméthy. Non-invasive sensor for the examination of the human or animal locomotor system. EPO patent 2186477-A1, 2010.

[38] A. Kecskeméthy and M. Hiller. An object-oriented approach for an effective formulation of multibody dynamics. *CMAME*, 115:287–314, 1994.

[39] L. Kuxhaus, P. J. Schimoler, J. S. Vipperman, and M. C. Miller. Effects of camera switching on fine accuracy in a motion capture system. *Journal of Biomechanical Engineering*, 131(1):014502, 2009.

[40] L. Lemieux, R. Jagoe, D. R. Fish, N. D. Kitchen, and D. G. T. Thomas. A patient-to-computed-tomography image registration method based on digitally reconstructed radiographs. *Medical Physics*, 21(11):1749–1760, 1994.

[41] G. Li, T. H. Wuerz, and L. E. DeFrate. Feasibility of using orthogonal fluoroscopic images to measure in vivo joint kinematics. *Journal of Biomechanical Engineering*, 126(2):313–318, 2004.

[42] M. Liang. Untersuchung von Einflussfaktoren manueller 2D-3D Registrierung dualer Fluoroskopie. Bachelor's Thesis, University of Duisburg-Essen, Duisburg, Jan 2019.

[43] D. D. Lichti, G. B. Sharma, G. Kuntze, B. Mund, J. E. Beveridge, and J. L. Ronsky. Rigorous geometric self-calibrating bundle adjustment for a dual fluoroscopic imaging system. *IEEE Transactions on Medical Imaging*, 34(2):589–598, Feb 2015.

[44] T.-W. Lu and J. O'Connor. Bone position estimation from skin marker coordinates using global optimisation with joint constraints. *Journal of Biomechanics*, 32(2):129 – 134, 1999.

[45] L. Lucchetti, A. Cappozzo, A. Cappello, and U. D. Croce. Skin movement artefact assessment and compensation in the estimation of knee-joint kinematics. *Journal of Biomechanics*, 31(11):977 – 984, 1998.

[46] B. Mariani, C. Hoskovec, S. Rochat, C. Büla, J. Penders, and K. Aminian. 3D gait assessment in young and elderly subjects using foot-worn inertial sensors. *Journal of Biomechanics*, 43(15):2999–3006, 2010.

[47] M. A. Masum, M. Pickering, A. Lambert, J. Scarvell, and P. Smith. Accuracy assessment of tri-plane B-mode ultrasound for non-invasive 3D kinematic analysis of knee joints. *BioMedical Engineering OnLine*, 13(1):122, 2014.

[48] MATLAB (version 9.3 (R2017b)). The MathWorks Inc., Natick, Massachusetts, 1984.

[49] D. L. Miranda, J. B. Schwartz, A. C. Loomis, E. L. Brainerd, B. C. Fleming, and J. J. Crisco. Static and dynamic error of a biplanar videoradiography system using marker-based and markerless tracking techniques. *Journal of Biomechanical Engineering*, 133(12):121002, 2011.

[50] M. B. Monagan, K. O. Geddes, K. M. Heal, G. Labahn, S. M. Vorkoetter, J. McCarron, and P. DeMarco. *Maple 10 Programming Guide*. Maplesoft, Waterloo ON, Canada, 2005.

[51] K. Niu, T. Anijs, V. Sluiter, J. Homminga, A. Sprengers, M. A. Marra, and N. Verdonschot. In situ comparison of A-mode ultrasound tracking system and skin-mounted markers for measuring kinematics of the lower extremity. *Journal of Biomechanics*, 72:134 – 143, 2018.

[52] K. Niu, J. Homminga, V. Sluiter, A. Sprengers, and N. Verdonschot. Measuring relative positions and orientations of the tibia with respect to the femur using one-channel 3D-tracked A-mode ultrasound tracking system: A cadaveric study. *Medical Engineering & Physics*, 57:61 – 68, 2018.

[53] C. Nüesch, E. Roos, G. Pagenstert, and A. Mündermann. Measuring joint kinematics of treadmill walking and running: Comparison between an inertial sensor based system and a camera-based system. *Journal of Biomechanics*, 57:32 – 38, 2017.

[54] A. Peters, B. Galna, M. Sangeux, M. Morris, and R. Baker. Quantification of soft tissue artifact in lower limb human motion analysis: A systematic review. *Gait & Posture*, 31(1):1 – 8, 2010.

[55] W. Pschyrembel. *Klinisches Wörterbuch*. Walter de Gruyter, 2011.

[56] D. K. Ramsey and P. F. Wretenberg. Biomechanics of the knee: Methodological considerations in the in vivo kinematic analysis of the tibiofemoral and patellofemoral joint. *Clinical Biomechanics*, 14(9):595 – 611, 1999.

[57] F. Ranjbaran, J. Angeles, and A. Kecskeméthy. On the kinematic conditioning of robotic manipulators. In *IEEE International Conference on Robotics and Automation*, volume 4, pages 3167–3172, Minneapolis, April 22-28 1996.

[58] J. A. Reinbolt, J. F. Schutte, B. J. Fregly, B. I. Koh, R. T. Haftka, A. D. George, and K. H. Mitchell. Determination of patient-specific multi-joint kinematic models through two-level optimization. *Journal of Biomechanics*, 38(3):621 – 626, 2005.

[59] C. Reinschmidt, A. Van Den Bogert, A. Lundberg, B. Nigg, N. Murphy, A. Stacoff, and A. Stano. Tibiofemoral and tibiocalcaneal motion during walking: External vs. skeletal markers. *Gait & Posture*, 6(2):98–109, 1997.

[60] J. G. Richards. The measurement of human motion: A comparison of commercially available systems. *Human Movement Science*, 18(5):589–602, 1999.

[61] M. Sati, J. de Guise, S. Larouche, and G. Drouin. Quantitative assessment of skin-bone movement at the knee. *The Knee*, 3(3):121 – 138, 1996.

[62] G. B. Sharma, G. Kuntze, D. Kukulski, and J. L. Ronsky. Validating dual fluoroscopy system capabilities for determining in-vivo knee joint soft tissue deformation: A strategy for registration error management. *Journal of Biomechanics*, 48(10):2181 – 2185, 2015.

[63] R. Stagni, S. Fantozzi, and A. Cappello. Double calibration vs. global optimisation: Performance and effectiveness for clinical application. *Gait & Posture*, 29(1):119 – 122, 2009.

[64] R. Stagni, S. Fantozzi, A. Cappello, and A. Leardini. Quantification of soft tissue artefact in motion analysis by combining 3D fluoroscopy and stereophotogrammetry: A study on two subjects. *Clinical Biomechanics*, 20(3):320 – 329, 2005.

[65] D. Stalling, M. Westerhoff, and H.-C. Hege. Amira: A highly interactive system for visual data analysis, 2005.

[66] S. Tadano, R. Takeda, and H. Miyagawa. Three dimensional gait analysis using wearable acceleration and gyro sensors based on quaternion calculations. *Sensors*, 13(7):9321–9343, 2013.

[67] S. Tashman and W. Anderst. In-vivo measurement of dynamic joint motion using high speed biplane radiography and CT: Application to canine ACL deficiency. *Journal of Biomechanical Engineering*, 125(2):238–245, 2003.

[68] S. Tashman, P. Kolowich, D. Collon, K. Anderson, and W. Anderst. Dynamic function of the ACL-reconstructed knee during running. *Clinical Orthopaedics and Related Research*, 454:66–73, 2007.

[69] S. Tedesco, A. Urru, A. Clifford, and B. O'Flynn. Experimental validation of the Tyndall portable lower-limb analysis system with wearable inertial sensors. *Procedia Engineering*, 147:208 – 213, 2016. The Engineering of SPORT 11.

[70] Tekscan pressure mapping sensor 5027. `https://www.tekscan.com/products-solutions/pressure-mapping-sensors/5027`. Accessed: 2019-02-01.

[71] The NAG C Library (Mark 25). The Numerical Algorithms Group (NAG), Oxford, United Kingdom www.nag.com.

[72] Y. Wen. Auswahl eines geeigneten Filters zur Bestimmung des dichtesten Sphäre-Ebenen-Projektionspunktes aus einer Druckverteilung. Bachelor's Thesis, University of Duisburg-Essen, Duisburg, Aug 2017.

[73] Y.-J. Weng, R. W.-W. Hsu, and W.-H. Hsu. Comparison of computer-assisted navigation and conventional instrumentation for bilateral total knee arthroplasty. *The Journal of Arthroplasty*, 24(5):668 – 673, 2009.

[74] M. Windolf, N. Götzen, and M. Morlock. Systematic accuracy and precision analysis of video motion capturing systems-exemplified on the Vicon-460 system. *Journal of Biomechanics*, 41(12):2776–2780, 2008.

[75] B. M. You, P. Siy, W. Anderst, and S. Tashman. In vivo measurement of 3-D skeletal kinematics from sequences of biplane radiographs: Application to knee kinematics. *IEEE Transactions on Medical Imaging*, 20(6):514–525, June 2001.

Die Reihen der Fortschritt-Berichte VDI:

1 Konstruktionstechnik/Maschinenelemente
2 Fertigungstechnik
3 Verfahrenstechnik
4 Bauingenieurwesen
5 Grund- und Werkstoffe/Kunststoffe
6 Energietechnik
7 Strömungstechnik
8 Mess-, Steuerungs- und Regelungstechnik
9 Elektronik/Mikro- und Nanotechnik
10 Informatik/Kommunikation
11 Schwingungstechnik
12 Verkehrstechnik/Fahrzeugtechnik
13 Fördertechnik/Logistik
14 Landtechnik/Lebensmitteltechnik
15 Umwelttechnik
16 Technik und Wirtschaft
17 Biotechnik/Medizintechnik
18 Mechanik/Bruchmechanik
19 Wärmetechnik/Kältetechnik
20 Rechnerunterstützte Verfahren (CAD, CAM, CAE CAQ, CIM ...)
21 Elektrotechnik
22 Mensch-Maschine-Systeme
23 Technische Gebäudeausrüstung

ISBN 978-3-18-329617-0